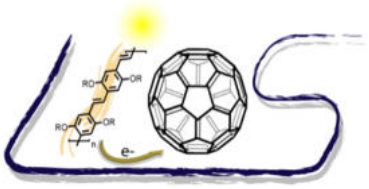

JOHANNES KEPLER
UNIVERSITY LINZ

Submitted by

Elisabeth Leeb

Submitted at

Institute of Physical Chemistry and Linz Institute for Organic Solar Cells

Supervisor

a. Univ. Prof. Markus Clark Scharber

Co-Supervisor

Univ. Prof. Martin Kaltenbrunner

May 2022

SYNTHESIS AND CHARACTERISATION OF PEROVSKITE NANOPARTICLES WITH LOW ENERGY EMISSION

Master Thesis

to obtain the academic degree of

Diplom-Ingenieurin

in the Master's Program

Chemistry and Chemical Technology

JOHANNES KEPLER UNIVERSITY LINZ
Altenberger Str. 69
4040 Linz, Austria
www.jku.at
DVR 0093696

JOHANNES KEPLER
UNIVERSITY LINZ

Statutory Declaration

I hereby declare that the thesis submitted is my own unaided work, that I have not used any sources other than those indicated and that all direct and indirect sources are acknowledged as references.

Linz, 03.05.22
Place, date

Elisabeth Leeb
Signature

Acknowledgement

First and foremost, I would like to thank my supervisor, Prof. Markus Scharber, for his guidance throughout this work. I truly appreciate all the time spent on measurements and discussions to further this thesis.

Furthermore, I want to express my gratitude to Prof. Niyazi Serdar Sariciftci, for inviting me to work at his institute and always being available for any helpful remarks during my scientific studies. In addition, I would like to thank Prof. Martin Kaltenbrunner, for his support of my work and Prof. Oliver Brüggemann, for offering me the use of his laboratory. I would also like to thank the whole team of the Institute of Polymer Chemistry for their kindness and swift help in all situations.

Moreover, I would like to thank Felix Mayr for his invaluable contribution to this thesis. Being able to compare results and discuss observations substantially improved the results of this work. I also want to thank Priv.-Doz.in Yolanda Salinas for her encouragement, helpful advice and insight.

Additionally, I am grateful for all the great people working at LIOS, who create such a welcoming environment, that coming to work is always enjoyable. In particular, I would like to thank Dominik Wielend for starting my curiosity about physical chemistry, Katarina Gugujonovic for sharing my fate of working on perovskites, as well as motivating me to never stop trying, and Jakob Hofinger for always being available for chats and discussions during much-needed snack breaks.

I also want to thank my friends who accompanied me along the journey of studying chemistry: Daniel Danner, Andreas Greul, Maximilian Hochrainer, Melissa Leibetseder, Andreas Miesenberger, Simon Oberfichtner, Lisa Öttl, Sarah Schwarz, and Florian Smrzka. Additionally, I want to thank Sarah Dornetshuber for being the best lab partner imaginable. Furthermore, I would like to thank my coffee boys, Alexander Felgel-Farnholz and (Christian) Kurt Wernecke, for brightening my day at the university and keeping me informed on any and all relevant developments, as well as Claudia Leimhofer, for her both helpful and entertaining commentary. Moreover, I would like to thank my partners in crime, Magdalena Fidler and Nadine Kleinbruckner, without whose help I would have never made it through the countless exams and numerous lab courses. Thank you all for your support and friendship!

Above all, I am utterly grateful to my boyfriend, Felix Leibetseder. Thank you for enduring the occasional monologue on my fascination with perovskites and for your input and curiosity in my scientific studies. I am so grateful to have met you. You improve my life every day!

Last but certainly not least, I would like to thank my parents and my stepdad, Robert. I really appreciate your support and interest in my studies. Thank you for being there for me and encouraging me in every area of my life.

Abstract

In recent years, hybrid organic-inorganic perovskite nanoparticles have been extensively studied for applications in opto-electronic devices due to their promising properties of high photoluminescence quantum yields (PLQY) and high colour purity over the whole visible spectrum. In this thesis, the synthesis of low energy emissive perovskite nanoparticles is reported using the ligand assisted re-precipitation method with the ligand system of *t*boc-lysine and hexanoic acid. Methylammonium-based mixed halide particles are produced to achieve red-emission, employing an iodide content of 33 %. The synthesis is carried out at atmospheric ambient conditions, followed by post-synthetic annealing of the thin film samples.

The synthesised mixed halide nanoparticles display a remarkable tolerance toward water as well as high stability under ambient conditions. The thin film samples show a mean emission maximum of 672 nm with a PLQY of 45 %. Furthermore, the particles are found to be homogeneous in terms of size, shape and composition and display a higher exciton binding energy than bulk material, confirming the quantum confinement effect. Fluorescence lifetime studies reveal no noticeable dependence on the iodide content.

Kurzfassung

Aufgrund der vielversprechenden Eigenschaften von hoher Photolumineszenz-Quantenausbeute (PLQY) und Farbreinheit über das gesamte sichtbare Spektrum wurden hybride organisch-anorganische Perowskit-Nanopartikel in den letzten Jahren eingehend für Anwendungen in optoelektronischen Geräten untersucht. In dieser Arbeit wird die Synthese von Perowskit-Nanopartikeln beschrieben, die im Niedrigenergiebereich emittieren. Zur Synthese wird die „ligand assisted re-precipitation“ oder auch LARP Methode verwendet, mit dem Ligandensystem von *t*boc-Lysin und Hexansäure. Mischhalogenidpartikel auf Methylammoniumbasis mit einem Iodidgehalt von 33 % werden hergestellt, um eine rote Emission zu erreichen. Die Synthese wird unter atmosphärischen Umgebungsbedingungen hergestellt, woraufhin die Dünnschichtfilme erhitzt werden.

Die synthetisierten, Halogenid-gemischten Nanopartikel zeigen eine bemerkenswerte Toleranz gegenüber Wasser sowie eine hohe Stabilität bei Umgebungsbedingungen. Die Dünnschichtproben besitzen ein mittleres Emissionsmaximum von 672 nm mit einer PLQY von 45 %. Darüber hinaus weisen die Partikel eine hohe Homogenität auf, sowohl in Bezug auf Größe, Form und Zusammensetzung. Durch Niedrigtemperatur Spektroskopie wurde eine höhere Exzitonenbindungsenergie als im Bulkmaterial gefunden, was auf einen Quanten-Confinement-Effekt hinweist. Untersuchungen der Fluoreszenzlebensdauer zeigen keine merkliche Abhängigkeit vom Iodidgehalt.

JOHANNES KEPLER UNIVERSITY LINZ

Table of contents

1. Introduction

In recent years, hybrid organic-inorganic lead halide perovskites have steadily gained popularity in various opto-electronic devices, most prominently in photovoltaics. Perovskite-based solar cells have already reached power conversion efficiencies larger than 25 %, with efficiencies steadily rising[1–3]. These values are primarily due to the remarkable optoelectronic properties of perovskites, such as high charge carrier mobility, high absorption of light, tuneable band gaps, and long diffusion lengths of charge carriers[3–5].

In contrast to the bulk material, perovskite nanoparticles (PNPs) are more feasible for an application in light-emitting diodes[4,6,7] or colour converters[8] due to their large photoluminescence quantum yields (PLQYs) and high colour purity with a small full-width at half-maximum (FWHM) of the fluorescence emission spectrum. As perovskites display a finely tuneable band gap, this high colour purity can be achieved over the whole visible spectrum.

However, the synthesis of PNPs with low energy, red emission, and a high PLQY has proven to be a challenge, with values being lower than their green emissive counterparts[9–12], due to structural instabilities of iodide-containing PNPs. This phenomenon has been known as the "perovskite red wall"[13–17]. Furthermore, while high fluorescence yields have been achieved in colloidal solutions, the PLQY of thin film samples and their stability at ambient conditions remains challenging, as thin film samples generally degrade within one week[11,18–21].

This thesis aims to synthesise mixed halide methylammonium perovskite nanoparticles (PNPs) using the well-established ligand-assisted reprecipitation (LARP)[22,23] method, with *t*boc-lysine and hexanoic acid as ligands. The synthesis parameters are adjusted to maximise the PLQY of PNP thin film samples. The resulting nanoparticles show remarkable tolerance towards water and high stability under ambient conditions.

1.1. Perovskites

Perovskite type minerals were first discovered by a Prussian scientist named Gustav Rose in 1839. He discovered and analysed a chlorite-rich skarn contained calcium titanium oxide ($CaTiO_3$) and named the new compound after the Russian mineralogist Count Lev A. Perovskiy[24,25]. The term "perovskite" is used to describe both the $CaTiO_3$ as well as the structural family[26]. Apart from oxide perovskites used in ferroelectric, piezoelectric, and dielectric application[25,27,28], halide perovskites are the most known and well-studied representative of this structural family due to them being a semiconductor material[25].

Halide perovskite materials are defined by their crystal structure. The three-dimensional crystal lattice comprises of BX_6^{4-} octahedra, which are connected at the corners, with the void created by the octahedron filled by an A^+ cation. The general structure of ABX_3 is shown in

Figure 1. For highly fluorescent perovskite nanoparticles, the A site is mainly made up of either caesium (Cs), methylammonium (MA), or formamidinium (FA) cations, while the B site is almost exclusively lead, with few exceptions using other divalent cations. The anionic X^- site is taken up by either a single halogen type, like chloride, bromide, fluoride or even a mixture of more than one halogen[29].

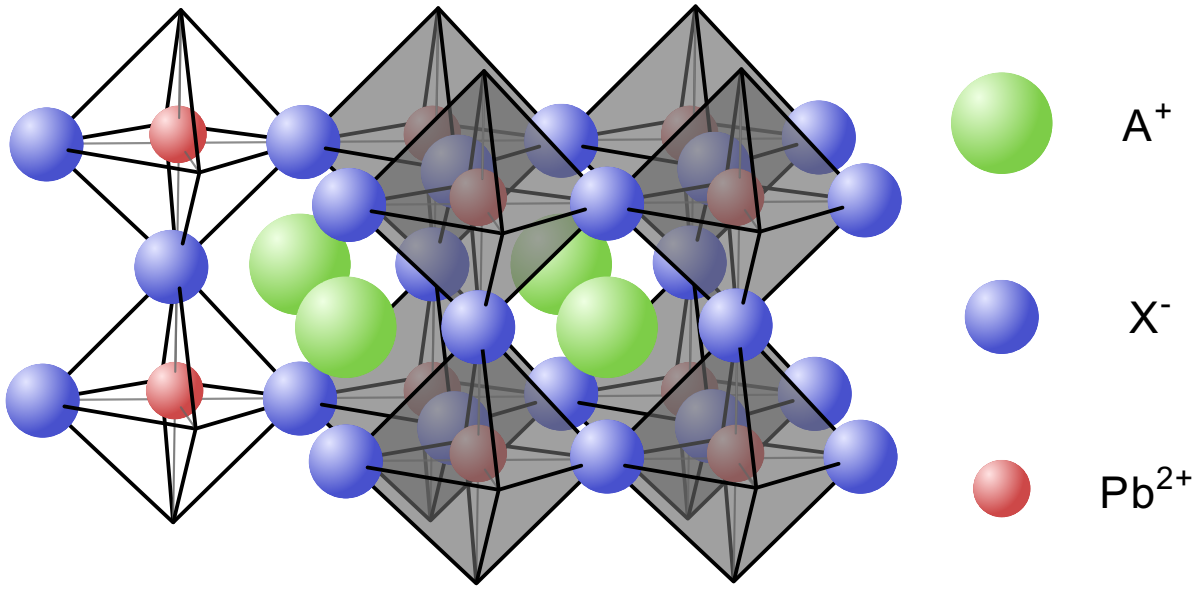

Figure 1: Schematic depiction of the ABX_3 structure of perovskites.

Whether or not a set of ions will form a perovskite structure is dictated by the space-filling ionic size of the individual components. The Goldschmidt's Tolerance Factor, depicted in **Equation 1**, is a measure of whether any composition will form a perovskite. It treats all ions as rigid spheres with a certain radius and sets these radii into relation. Empirically, it was observed that 3D perovskite structures display a Goldschmidt Factor of $0.8 \leq t \leq 1.0$ [30].

$$t = \frac{r_A + r_X}{\sqrt{2}\,(r_B + r_X)} \qquad \text{(Eq. 1)}$$

with: r_A = radius of A cation

r_B = radius of B cation

r_X = radius of halide anion

Furthermore, charge balance has to be achieved as well. In most established perovskites, A is a monovalent cation, while B is a divalent cation. However, this is not strictly necessary, as the +2 charge of B can also be achieved by implementing an equal number of +1 and +3 cations, yielding an overall charge of +2. This configuration is employed in $CsAuI_3$, where a disproportionation of Au into +1 and +3 charged states is observed, accounting for a net charge of +2[31].

Apart from the described three-dimensional structures, lower dimensions of perovskite

structures exist as well. These do not conform as rigidly to the Goldschmidt's Tolerance Factor as the parent structure. For example, there are no known constraints for the intercalated A cation in a two-dimensional perovskite derivate, while no size restrictions apply for zero-dimensional octahedral clusters[30,32].

The high PLQY displayed by PNPs is a consequence of the remarkable tolerance to defects of the perovskites. As it is energetically not beneficial to entirely displace ions within the crystal lattice, deep traps are almost completely absent[17,33]. Defects in the lattice are mainly formed due to vacancies, which only form shallow traps and show less impact on radiative recombination. Improved passivation of the surface of the nanocrystals with ligands further reduces the occurrence of trap states and depletion of photoluminescence[9]. Due to the high surface-to-volume ratio in nanoparticles, surface passivation is crucial for maximising the PLQY. For this purpose, ligands are used, which decorate the surface and thus stop particle growth to stabilise the particles. As this termination of crystal growth fundamentally affects the material's property, ligand engineering may be used to influence the resulting nanoparticles[23,34]. In general, carboxylic acids and long-chain amine ligands are used to passivate PNPs[9,35].

However, PNPs are also characterised by high instability and sensitivity towards water, oxygen, and heat. Due to their highly ionic nature, solvents such as water or polar organic solvents can fully disintegrate most perovskite materials[36,37]. To protect against such degradation, encapsulation into matrix materials has been used to enhance the lifetime of perovskite-based devices. As matrix materials, a wide variety such as polymers, paraffin, or silica coatings have been suggested[38–43].

Furthermore, due to the low energy of formation, perovskites, especially MA-based ones, suffer from thermal instability as the compound degrades to the volatile methylammonium and the hydrogen halide. This decomposition accelerates the hydration and thus the complete dissociation of the structure, which often occurs during purification or isolation processes[13,35]. Apart from a temperature-induced dissociation, this process may also be triggered through the presence of oxygen in a photo-oxidation reaction[37].

A further problem has been observed in mixed halide perovskites, which employ more than one different halide ion at the X position in the crystal lattice. In such systems, halide migration is observed, most prominently under constant illumination. With increasing illumination time, the halides separate into two individual pure phases, resulting in a low energy and a high energy emission and absorption. When halting the illumination, these anions migrate back to their original position, forming the same composition present in the initial state[35,44]. Ion migration has been observed in both bulk as well as nanosized perovskites and is often found to hinder device efficiency as well as the overall lifetime of perovskite-based electronics[45–47].

1.2. Synthesis approach for low energy emissive perovskites

Synthesis of low energy, red emissive PNPs has been predominately achieved by synthesising $CsPbI_3$ nanoparticles through hot injection with subsequent anion exchange. Here, a perovskite precursor is quickly injected into Cs-oleate, which is heated to 150 - 200 °C under an argon atmosphere. After a certain time, the reaction is quenched by rapidly cooling the solution, and the particles are isolated[35]. To synthesise $CsPbI_3$ PNPs, bromide particles are created through hot injection, and the halide is later exchanged by stirring the nanoparticles in an iodide-rich solution.

Using this method, *Bi et al.*[10] synthesised $CsPbI_3$ colloidal solutions, which showed a PLQY value of 83 % at an emission maximum of 667 nm. However, low ambient stability was observed. Thin film samples were produced by *Akkerman et al.*[48] with an emission maximum of 684 nm and a yield of 15 %, as well as by *Chiba et al.*[7] with a hypsochromically shifted emission of 649 nm and a PLQY of 26 %. In order to stabilise the created nanoparticles, *Guhrenz et al.*[8] immobilised the particles on potassium salts with subsequent embedding in silicone, reaching a remarkable PLQY of 79 % at an emission of 669 nm. Direct synthesis of $CsPbI_3$ nanoparticles through hot injection has also been achieved, resulting in a slightly lower emission maximum at 626 nm and a PLQY of 42 %[40], while direct synthesis by spin-coating the precursor onto a substrate did not prove to be effective, only reaching 15 % PLQY[49].

In contrast to all inorganic PNPs, organic-inorganic hybrid perovskites are synthesised using various methods. A top-down synthesis has been implemented for $MAPbI_3$ nanoparticles, where precursor materials are ground together in a mortar until PNPs are formed[11]. Sonication is used to decrease the particle size and form nanoparticles in a different approach, as demonstrated by *Huang et al*[50]. However, low stabilities hinder this synthesis method, as PLQY values decay within days due to insufficient surface passivation of the PNPs.

An interesting variation of the LARP method has been performed by *Hassan et al.*[6,12], where methylamine gas is used to generate a precursor, which is then injected into heated toluene. The nanoparticles are later subjected to a ligand exchange, boosting the PLQY to values above 60 %. Other LARP methods have been implemented successfully however, still suffering from stability issues under ambient conditions. While high values are achieved for colloidal solutions and embedded particle films, no satisfying values are reported for neat thin film samples[19,51].

Compared to MA-based PNPs, FA-based red emissive nanoparticles have been reported at lower PLQY values. While very high emission maxima above 770 nm have been reported[18], only low quantum yields have been achieved for thin film samples[4,5,52]. In colloidal solutions, *Levchuk et al.*[20] reported PLQY values for $FAPbI_3$ of 55 % at an emission maximum of 740 nm, with no report concerning thin film samples.

Noticeably, regardless of the synthesis method, low energy emissive PNPs are almost exclusively synthesised using oleic acid and oleylamine as the ligand system. Oleic acid is known to stabilise PNPs in solution and suppress aggregate formation[35]. Furthermore, the ligand system can undergo an acid-base reaction, resulting in oleate and oleylammonium, which may further react with any other species present in the precursor solution. Thus, a multitude of compounds may bind to the particle surface and thus passivate it more efficiently[53].

2. Experimental

2.1. Preparation of Precursor Solutions

The following synthesis was adapted from the general procedure described by *Jancik Prochazkova et al*[22]. For any composition of PNPs, a 0.34 mM solution of lead halide (lead bromide, $PbBr_2$ or lead iodide, PbI_2) and a 0.38 mM solution of the organic cation (methylammonium bromide, MABr; methylammonium iodide, MAI; formamidinium bromide, FABr or formamidinium iodide, FAI) are prepared by dissolving the appropriate amount of salt in anhydrous dimethylformamide (DMF).

Subsequently, 100 µL (0.034 mmol, 1 equiv.) of the lead solution are added to 6.7 mg (0.027 mmol, 0.8 equiv.) of *t*boc-lysine and 100 µL (0.037 mmol, 1.1 equiv.) of the solution containing the organic cation. Furthermore, 40 µL (0.320 mmol, 9.4 equiv.) hexanoic acid are added to the precursor solution, which is subsequently filled up to a total volume of 1.25 mL with DMF. If not stated otherwise, the precursor is adjusted to contain 19.6 µL (1.090 mmol, 32 equiv.) of ultrapure water.

The precursor solutions are left to stir in a fumehood at least overnight at room temperature before use.

A schematic depiction of the precursor preparation can be found in **Figure 2**.

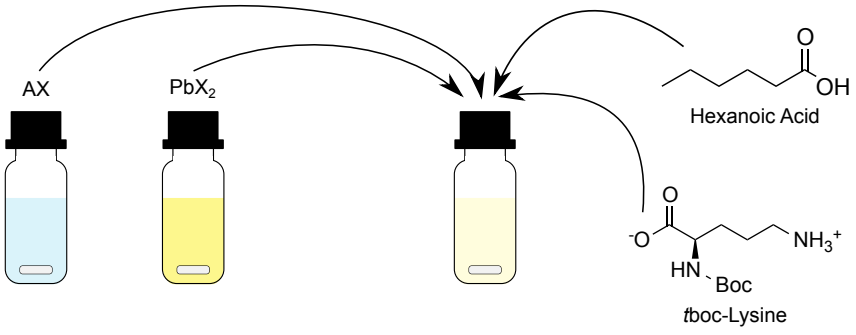

Figure 2: Schematic depiction of the preparation of the precursor solutions.

2.2. Preparation of PNP Thin Films and Solutions

The general procedure is described hereafter, which was used if not otherwise indicated.

To precipitate the nanoparticles, 12.5 mL of previously dried toluene (molecular sieve, 3 Å) are cooled in an ice bath to approximately 5 °C. While stirring, 75 µL precursor solution are added to the chilled toluene, which is then stirred for 2 minutes.

A glass slide (0.9 × 0.9 cm) was thoroughly cleaned using various organic solvents (acetone, isopropanol), plasma-treated (O_2, 5 minutes) and placed at the bottom of a centrifugation tube. The colloidal solution is slowly added to the centrifugation tube, after which it is centrifuged at 5000 rpm for 5 minutes, resulting in the deposition of the PNPs onto the glass slide. Using a Pasteur pipette, the supernatant is carefully removed, and the film is put in a vial and dried under a toluene atmosphere. The remaining particles at the bottom of the centrifugation tube are redispersed in 2 mL of toluene using an ultrasonic bath to yield colloidal solutions.

After the PNP thin film on top of the glass slide is dried, it is placed on a hot plate at 120 °C. After 5 minutes of annealing time, the film is removed and stored in a glass vial under ambient conditions.

A schematic depiction of the synthesis is depicted in **Figure 3**.

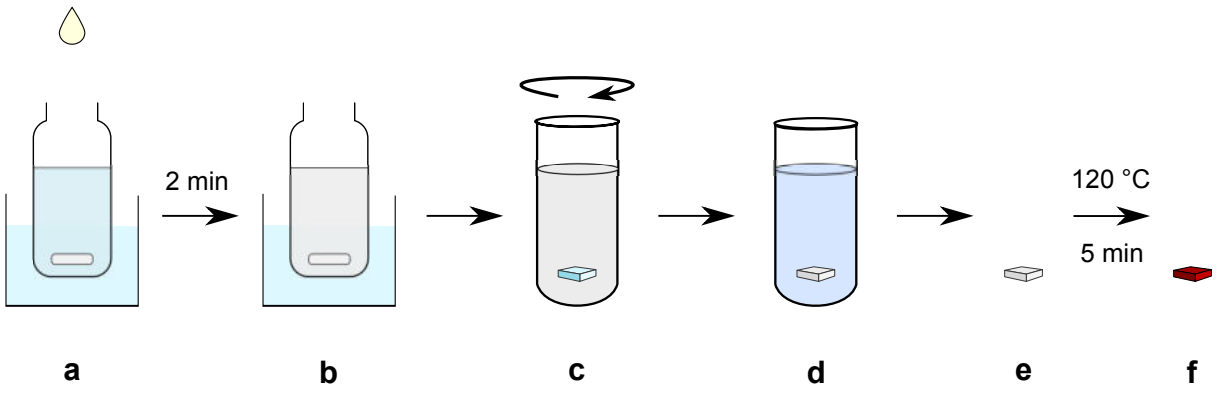

Figure 3: Schematic depiction of the synthesis of perovskite nanoparticle thin films. **a)** Injection of precursor solution into chilled toluene, **b)** solution is stirred for 2 minutes, **c)** colloidal solution is centrifuged, **d)** particles deposit on glass slide, **e)** toluene is removed and **e)** particles are annealed at 120 °C for 5 minutes inducing a colour change.

2.3. General Characterisation Methods

Photoluminescence excitation as well as absorption were measured with a PTI QuantaMaster 40 equipped with two monochromators on both the excitation and emission channels. All spectra are corrected for the detector response and the spectral output of the excitation laser. The samples were measured as thin films at room temperature.

PLQY values were determined using a Hamamatsu Photonics A9924-06 integrating-sphere. The sphere was operated with an L9799-01 continuous mode Xe lamp, a C8849 lamp power supply, an A10080-01 monochromator and a PMA-12 photonic multi-channel analyser at an excitation wavelength of 415 nm for bromide rich particles and 475 nm for iodide rich particles. The measurements were carried out by Markus Scharber (Johannes Kepler University, Linz).

Magnified images were obtained using a Nikon Eclipse LV100ND optical microscope. Images were taken at a magnification of 10x and 40x using Nikon LU Plan Fluor objectives. The images were obtained either in dark field mode with an external UV source at 254 nm or a fluorescence filter.

Low-temperature photoluminescence measurements were performed in a Quantum Design PPMS (Physical Property Measurement System) DynaCool. A 405 nm Coherent OBIS laser was used as an excitation source for bromide rich particles, while a 488 nm Coherent OBIS laser was used for iodide rich particles. Using optical fibre cables, both lasers were coupled into and out of the PPMS sample chamber. Furthermore, an Oxford Instruments Andor iStar CCD detector was used, coupled with an Oxford Instruments Andor Shamrock monochromator. To block incident laser light from reaching the detector, longpass filters were put in front of the aperture. Each set of measurements was taken at constant excitation energy.

Time-resolved spectroscopy was measured in an Oxford Instruments OptistatDry Cryostat equipped with an Oxford Instruments Mercury iTC temperature controller. The sample chamber was put under a high vacuum using a Pfeiffer Vacuum Turbomolecular pump. An NKT Photonics SuperK Extreme High Power Supercontinuum White Light Laser was used as an excitation source at a mean laser power of 0.1 to 1 mW, which was equipped with a Photonetc LLTF contrast monochromator. The laser power was adjusted to yield the desired ratio of incoming and detected counts. Measurements were performed at 4, 50, 100, 200 and 295 K. Using the low-temperature spectroscopy setup, the emission maximum was determined, and a DeltaNu DNS-300 monochromator was used to adjust for the specific emission wavelength. Incident photons were detected using a Becker & Hickel PMC-100-1 photomultiplier tube. The measurements were performed by Markus Scharber (Johannes Kepler University, Linz).

3. Results and Discussion

3.1. Compositional Screening

As the most common method of synthesising low energy emissive PNPs is an anion exchange synthesis, a proof-of-concept experiment using the ligand system *t*boc-lysine and hexanoic acid was performed. Given that bromide is the dominant binding species in mixed

halide perovskite systems, with a substantially larger tendency of complexation with lead than iodide[54], fully iodide particles were synthesised and redispersed in toluene alongside an excess of both $PbBr_2$ and MABr and stirred for up to 24 hours. At most, an emission maximum of 702 nm was achieved, which is nowhere near the emission maximum of fully bromide PNPs at around 500 nm. Therefore, ion exchange in the opposite direction, from bromide to iodide, was deemed not feasible, and a direct synthesis approach was adapted to generate red emissive particles.

3.1.1. Methylammonium as Cation

To start with, methylammonium was chosen as the A-type cation for the synthesis. Particles containing MABr were produced with a successively decreasing ratio of $PbBr_2$ to PbI_2. Once only PbI_2 was used in the synthesis at 66 % iodide content, MABr was steadily substituted for MAI. The photoluminescence spectra, as well as emission maximum and PLQY values, are depicted in **Figure 4**.

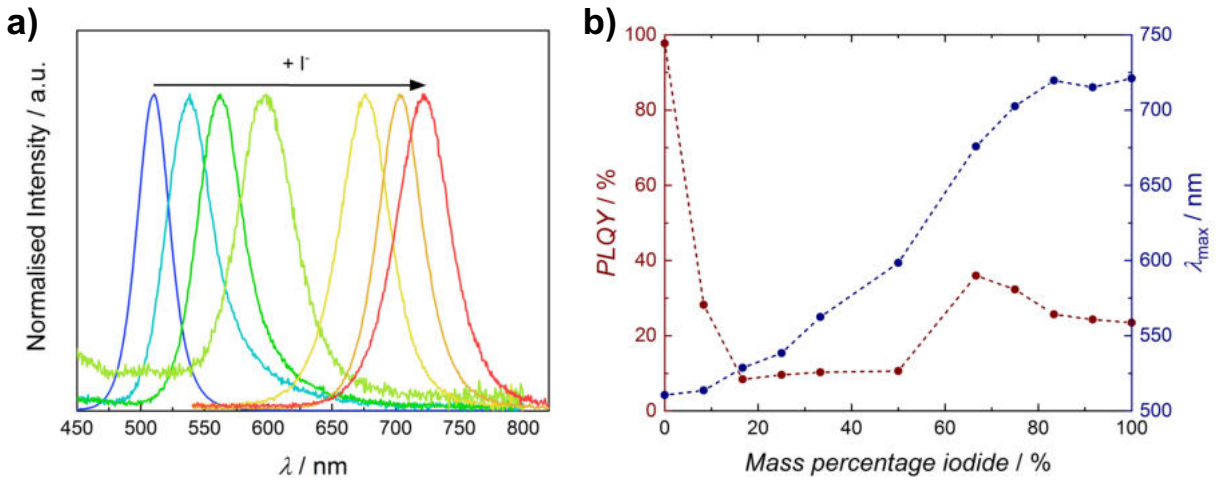

Figure 4: a) Photoluminescence spectra of perovskite nanoparticles fabricated with an increasing amount of iodide (starting with MABr and PbX_2), and corresponding **b)** PLQY and emission maxima against mass percentage of iodide.

When looking at **Figure 4a**, a progressive bathochromic shift with increasing iodide content can be seen. However, this increase does not happen linearly, as is evident when observing **Figure 4b**. A steeper increase in emission maximum as a function of iodide content is observed between 50 % and 66 %, as a majority of the X halide position is occupied by iodide. Furthermore, the PLQY value depicts a local maximum around 66 %, at a composition of purely MABr and PbI_2. These results indicate that when synthesising particles with a smaller band gap and a lower energy emission, only introducing two types of halide salts like MABr and PbI_2 seems to create a perovskite structure with fewer crystalline defects and thus fewer trap states, resulting in a higher PLQY value as compared to using a mixture of three or more salts.

To investigate the influence of the cation on which the iodide is introduced into the PNPs, a similar experiment was implemented using $PbBr_2$ and a varying ratio of MABr and MAI. The results are depicted in **Figure 5**.

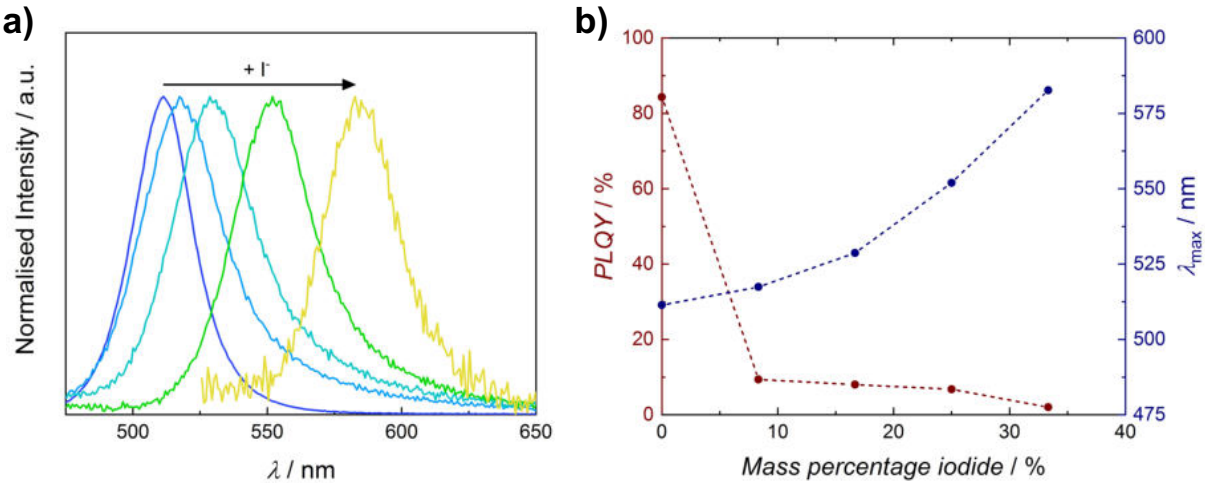

Figure 5: a) Photoluminescence spectra of perovskite nanoparticles fabricated with $PbBr_2$ and increasing amounts of MAI, and corresponding **b)** PLQY and emission maxima against mass percentage of iodide.

As shown in **Figure 5a**, varying the halide content by increasing the amount of MAI while decreasing MABr once more led to a bathochromic shift. However, when comparing the iodide content in these PNPs, as depicted in **Figure 5b**, with the iodide content in the PNPs synthesised by substituting $PbBr_2$ with PbI_2, seen in **Figure 4b**, it is noticeable that the bathochromic shift is slightly larger. Furthermore, the PLQY of the resulting nanoparticles drops off more rapidly when substituting MABr as compared to $PbBr_2$. For better comparison, the results are listed in **Table 1**.

Table 1: Comparison of emission maxima and PLQY of PNPs with increasing mass percentage of iodide.

	MABr with PbX_2		**MAX with $PbBr_2$**	
***wt%* Iodide / %**	***PLQY* / %**	**λ_{max} / nm**	***PLQY* / %**	**λ_{max} / nm**
0.0	97.7	511	94.3	511
8.3	28.2	514	9.4	517
16.7	8.4	529	8.0	529
25.0	9.6	538	6.8	552
33.3	10.3	562	2.0	583

As can be seen from **Table 1** at 33 % iodide content, the particles introducing iodide using lead as cation still retain a PLQY of 10.3 % while emitting at an emission maximum of 562 nm. Comparing these results to the nanoparticles synthesised using MAI, only a PLQY of 2.0 % could be achieved while emitting at a slightly red shifted wavelength of 583 nm. However, even

comparing the particles which emit at a comparable wavelength of 562 (MABr with PbX_2) and 552 nm (MAX with $PbBr_2$), the particles containing MAI still feature a lower quantum yield.

Interestingly, at the same iodide content present in the precursor solution, the resulting particles show differing emission maxima of up to 21 nm (83 meV) variation. This shift in emission might indicate a difference in the size of the PNPs. However, as has been stated in literature[54,55], due to the difference in the coordination of bromide and iodide with lead, the ratio employed in the precursor solution does not necessarily reflect the ratio of halides present in the resulting nanoparticles. Therefore, this bathochromic shift between the PNPs fabricated using PbI_2 and MAI might be due to a difference in the coordination of iodide to the lead centre.

Nevertheless, as the main focus of this thesis is the maximisation of the PLQY of red emissive nanoparticles, the difference between these two routes of synthesis was not further investigated, as the fabrication using PbI_2 and MABr seems the most promising.

3.1.2. Formamidinium as Cation

Apart from MA-based PNPs, FA was also chosen as a suitable cation for synthesising low energy emissive PNPs, as various groups report the successful synthesis of such particles[4,5,18]. Furthermore, the synthesis procedure employed in this work was proven to produce $FAPbBr_3$ PNPs with a PLQY of up to 100 %[56]. Thus, nanoparticles were synthesised using FABr with a varying ratio of $PbBr_2$ and PbI_2. The results are depicted in **Figure 6**.

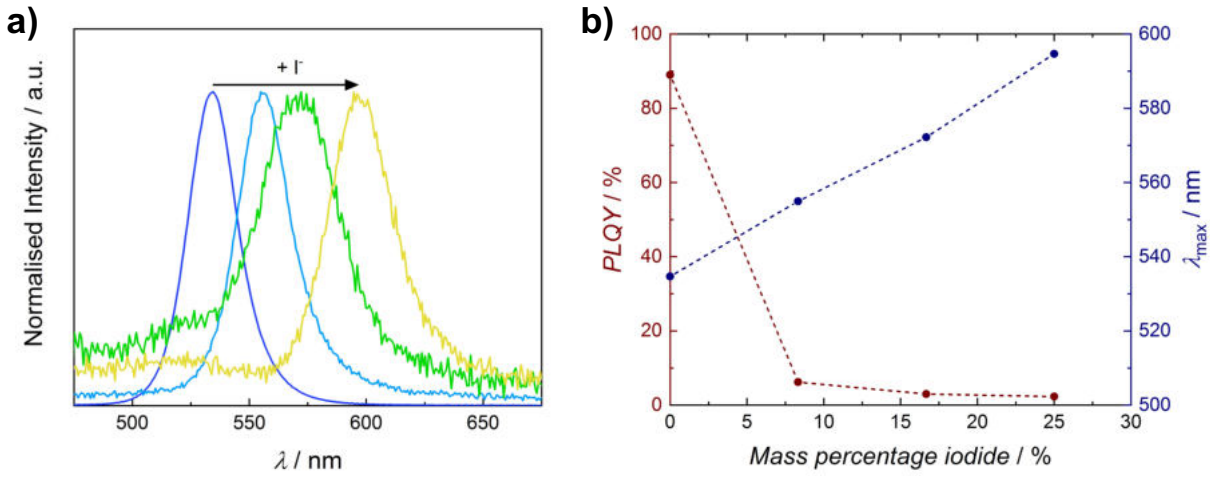

Figure 6: a) Photoluminescence spectra of perovskite nanoparticles fabricated with FABr and increasing amounts of PbI_2, and corresponding **b)** PLQY and emission maxima in dependence of mass percentage of iodide.

As shown in **Figure 6a**, PNPs based on FA showed a substantial bathochromic shift of 60 nm (234 meV) at an iodide content of merely 25 %, which was only achieved for MA-based nanoparticles at iodide contents above 33 %. However, as becomes immediately apparent

from the results plotted in **Figure 6b**, the PLQY drops off steeply to the point where FA-based nanoparticles containing 33 % iodide did not show any fluorescence.

Nevertheless, further particles have been synthesised using $PbBr_2$ with a varying ratio of FABr and FAI, successively increasing the iodide content. A roughly equal shift in emission was observed from these particles, yet the PLQY decreased even more rapidly, as a FA-based PNP at an iodide content of 8.3 % barely depicted a PLQY of 5.3 %. Thus, it was concluded that FA-based nanoparticles were not suitable to produce red emissive PNPs using the chosen synthesis procedure as well as the ligand system.

3.2. Influence of Synthesis Parameters

Several synthesis parameters have been considered and optimised to maximise the PLQY of the red emitting PNPs. Given that extensive work on $MAPbBr_3$ nanoparticles has already been performed by our group[22,23,56–58], these PNPs have been used as a reference system for the mixed halide perovskites.

3.2.1. Precipitation Temperature

Various reports in literature have shown an influence of the precipitation temperature on the optical properties of the resulting nanoparticles[23,59]. To ensure a stable temperature, an ice bath or oil bath was used respectively, with the temperature being varied from 5 to 70 °C. Toluene was placed in the tempered medium and stirred heavily for 15 minutes, after which the precursor was injected and left to stir.

When precipitating $MAPbBr_3$ nanoparticles, a colour change of the solution was visible at every temperature, as can be seen in **Figure 7**. However, interestingly, the intensity of the colour significantly increased with rising temperature, developing from a very faint green colour at 5 °C to a brightly coloured solution at 70 °C.

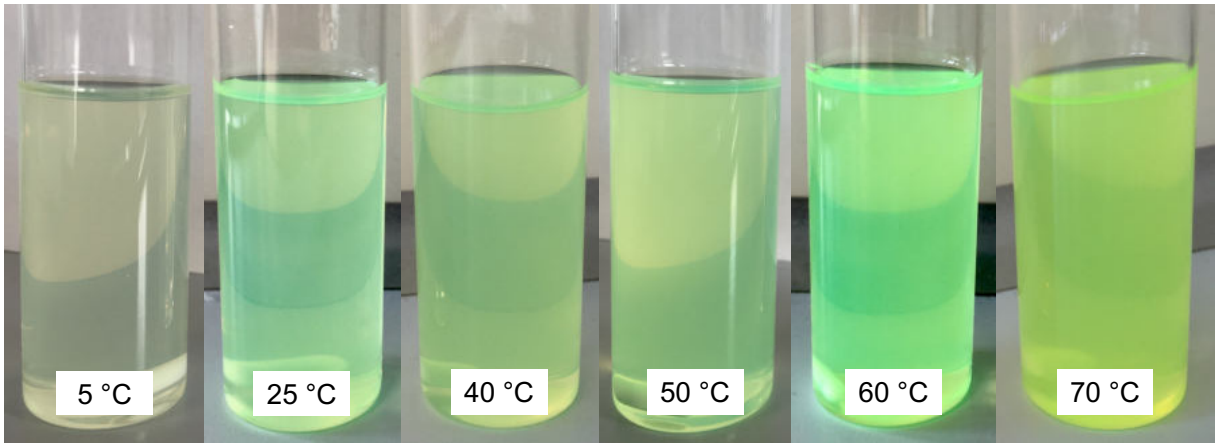

Figure 7: Colour change during the precipitation of $MAPbBr_3$ nanoparticles with increasing temperature.

In order to compare the resulting nanoparticles, all relevant spectroscopic characteristics of the thin film samples are listed in **Table 2**.

Table 2: Spectroscopic characteristics of $MAPbBr_3$ thin film samples, precipitated at varying temperatures.

***T* / °C**	***PLQY* / %**	**λ_{max} / nm**	***FWHM* / nm**
5	54	488	36
25	67	502	30
40	80	502	27
50	83	501	26
60	91	505	25
70	78	514	23

As can be seen in Table 2, the emission maximum is increasingly bathochromically shifted with rising precipitation temperature, with a total shift of 26 nm (130 meV) at 70 °C. Furthermore, an increase in PLQY is observed, from 54 % to an impressive value of 91 % at 60 °C, which decreases again at 70 °C. It seems as though an increase in temperature is favourable to the formation of the nanoparticles up to a certain threshold temperature. Alongside the decrease in PLQY, a noticeable jump in emission maximum is also visible at this temperature.

As already suggested by the increased intensity of the green colour formed after injecting the precursor into toluene, thicker, more densely packed films were formed with increasing temperature. Surprisingly, a linear decrease of FWHM with increasing temperature is observed. It may be concluded that at higher temperatures of 70 °C, more uniform particles are formed, thus emitting in a narrower range.

It seems as though raised temperatures enhance the formation of the perovskite lattices while lowering the probability of lattice defects and, consequently, trap formation. However, at 70 °C, the formation of highly emissive nanoparticles is no longer favourable, as the decrease in PLQY and the step increase in emission maximum while maintaining a narrow FWHM suggests the beginning formation of bulk material rather than nanoparticles[60].

An image of the $MAPbBr_3$ nanoparticle thin film samples prepared at varying precipitation temperatures is depicted in **Figure 8**.

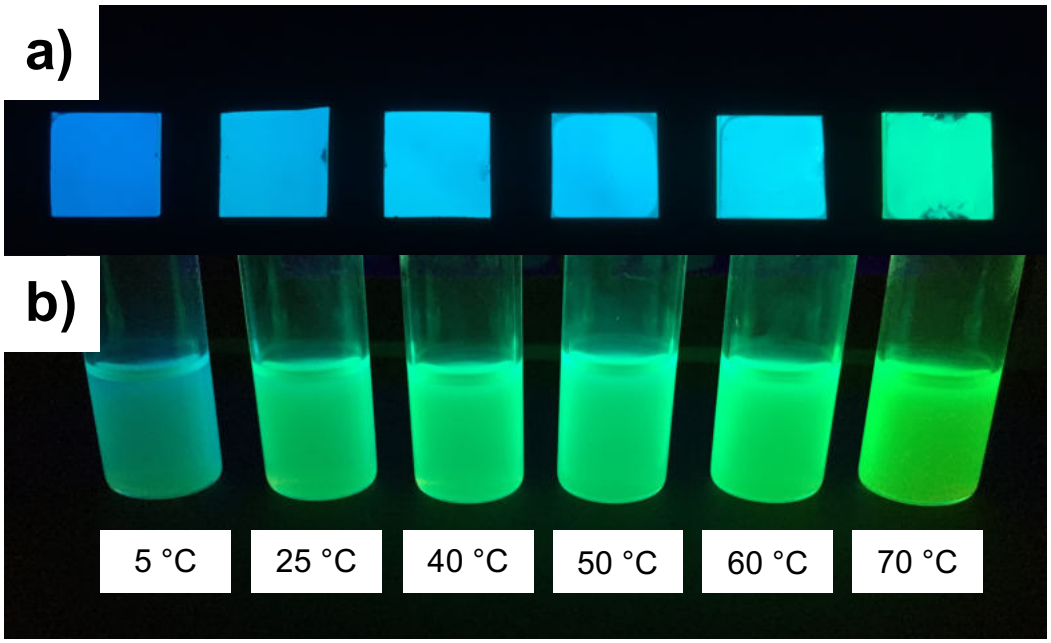

Figure 8: a) $MAPbBr_3$ thin films and **b)** solutions with increasing precipitation temperature illuminated by a UV-lamp (254 nm).

As shown in **Figure 8a**, the bathochromic shift with increasing temperature is clearly visible, even to the naked eye. Furthermore, the thin film precipitated at 5 °C shows a more uniform and smoother surface than the films precipitated at temperatures higher than 50 °C. Additionally, the PNP dispersions depicted in **Figure 8b** showed quite varying behaviour in sedimentation. While beginning sedimentation was already observed after one minute in samples precipitated at temperatures higher than 40 °C, the particles precipitated at lower temperatures stayed in suspension much longer, with slight sedimentation only visible after approximately 5 minutes. This behaviour may indicate agglomerate formation at higher precipitation temperatures in addition to the formation of larger nanoparticles, while fewer agglomerates form at lower temperatures.

Similar trends were observed when precipitating mixed halide $MAPbBrI_2$ nanoparticles, with 66 % iodide content, at varying temperatures. At 5 °C, as well as at room temperature, no red colour was observed during precipitation, with the colour slowly developing when raising the temperature, as shown in **Figure 9**. Also, flocculation was observed at room temperature, as large, white particles formed, which were not present at other temperatures.

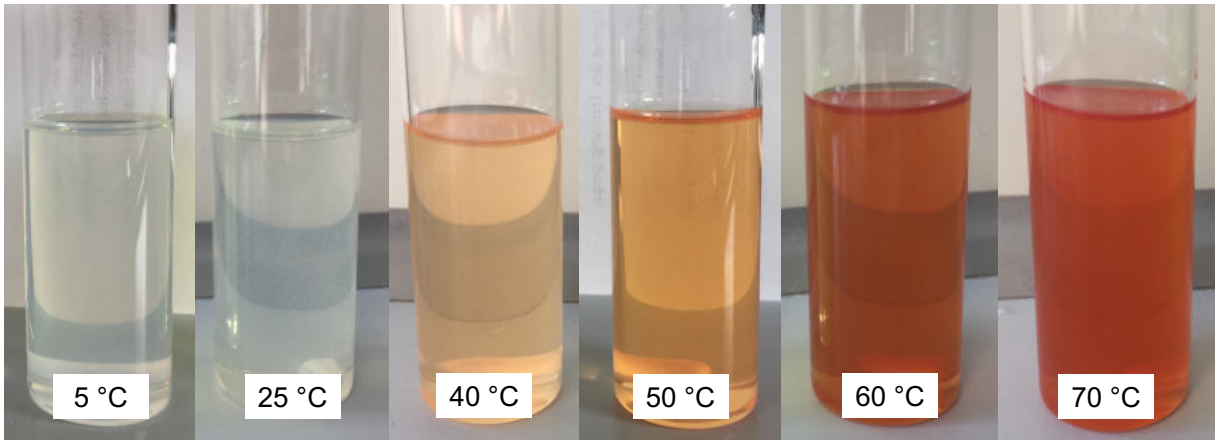

Figure 9: Colour change during the precipitation of $MAPbBrI_2$ nanoparticles with increasing temperature.

As no fluorescence was visible when precipitating the nanoparticles below room temperature, all resulting thin film samples were annealed post centrifugation and drying. All samples were placed on a hot plate set to 120 °C for approximately 10 seconds. The difference in appearance can be seen in **Figure 10**.

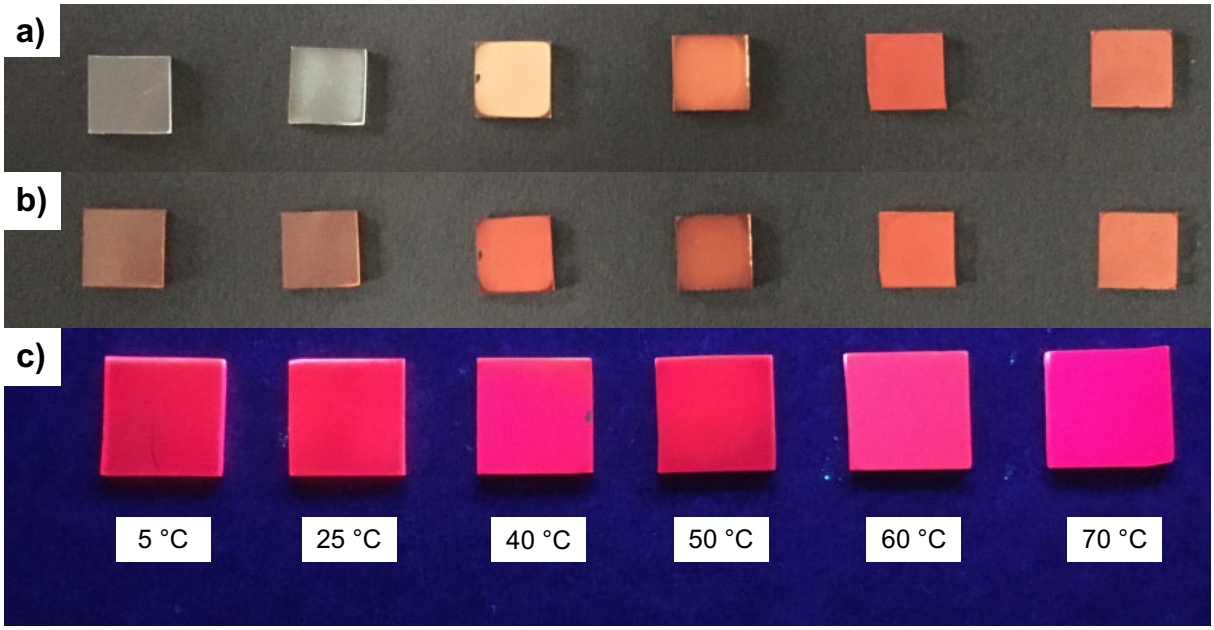

Figure 10: $MAPbBrI_2$ thin films with increasing precipitation temperature **a)** prior and **b)** post annealing as well as **c)** post annealing, illuminated by a UV-lamp (254 nm).

As shown in **Figure 10a**, the samples precipitated at 5 and 25 °C showed no colour prior to annealing, merely displaying a milky white appearance. After all samples were annealed at 120 °C, the samples precipitated at 5, 25 and 40 °C significantly changed in colour, turning a more noticeable orange colour, as can be seen in **Figure 10b**. Furthermore, the samples precipitated at 25 °C or lower showed a translucent appearance. In contrast, the samples precipitated at higher temperatures did not appear to be sheer, with an opaque, milky colour

and only occasional transparent areas at the edge of the samples. When illuminated by a UV-lamp (254 nm), no difference in fluorescence intensity or colour is visible between the opaque and transparent areas, as shown in **Figure 10c**.

To better compare the optical properties between the different samples, PLQY, emission maxima, and FWHM values are listed in **Table 3**.

Table 3: Spectroscopic characteristics of $MAPbBrI_2$ thin film samples, precipitated at varying temperatures.

***T* / °C**	***PLQY* / %**	**λ_{max} / nm**	***FWHM* / nm**
5	47	671	45
25	42	674	43
40	20	656	45
50	23	667	46
60	27	672	43
70	35	671	44

As can be seen in **Table 3**, the highest PLQY value of 47 % was achieved when precipitating the nanoparticles at the lowest temperature of 5 °C, followed by annealing at 120 °C post synthesis. The quantum yield dropped off at 40 °C, steadily rising again to 35 % at 70 °C. Apart from this development, no other spectroscopic characteristics follow any discernible trends. No noteworthy difference is found in FWHM, and no effect worth mentioning is found concerning emission maximum either, as a nonlinear fluctuation of merely 7 nm (18 meV) is seen, exempting the value at 40 °C, which deviates more strongly. According to these data, precipitating the nanoparticles at low temperatures followed by annealing to induce the colour change yields the best results and was therefore adopted as the standard synthesis. Similar behaviour has been seen in literature, where particle growth from nanoparticles to bulk material was found during post-synthetic annealing[61].

3.2.2. Annealing Temperature and Time

In order to determine the optimum annealing temperature, several batches of $MAPbBrI_2$ nanoparticles were precipitated at 5 °C and annealed at different temperatures, ranging from 70 to 160 °C. All samples were kept on the hot plate until a visible colour change occurred, which took approximately 10 seconds. The results for PLQY and emission maximum are depicted in **Figure 11**.

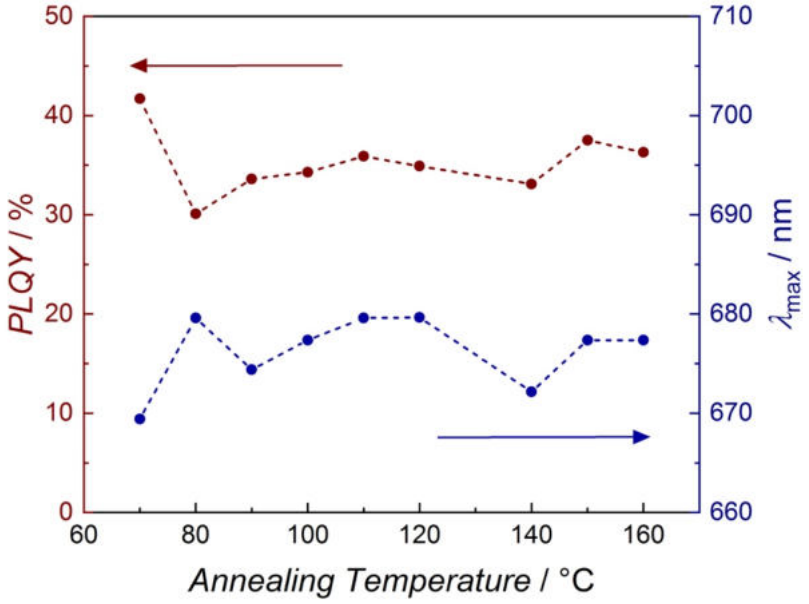

Figure 11: PLQY and emission maxima of $MAPbBrI_2$ thin films with increasing annealing temperature.

As can be seen from **Figure 11**, no apparent optimum annealing temperature could be found, as both the PLQY as well as the emission maximum showed some fluctuation. The best quantum yield could be achieved at 70 °C however, at this temperature, the lowest emission maximum of 669 nm was observed. Therefore, an annealing temperature of 120 °C was used for all PNPs fabricated according to the general synthesis.

Furthermore, the ideal time for annealing was also investigated. Multiple samples were placed on the hot plate for different periods, varying from 10 seconds to 60 minutes. The results are listed in **Table 4**.

Table 4: Spectroscopic characteristics of mixed halide perovskite thin films annealed at 120 °C for an increasing amount of time.

***t* / min**	***PLQY* / %**	**λ_{max} / nm**	***FWHM* / nm**
0.17	34	664	40
5	47	669	40
10	43	671	40
30	45	676	41
60	0	-	-

As shown in **Table 4**, a significant increase in PLQY occurs when annealing the nanoparticles for a slightly longer time. Furthermore, the emission maximum is successively shifted to lower energies and higher wavelengths as the annealing time increases. However, after 30 minutes, the colour of the thin film samples considerably decreases in intensity, likely due to a degradation of the perovskite structure into volatile products[13,35,62], decreasing the thickness of the thin film sample. After 60 minutes, no fluorescence is measurable, as the perovskite structure seems to have fully degraded.

To characterise this difference further, the films were observed under the optical microscope, as can be seen in **Figure 12**.

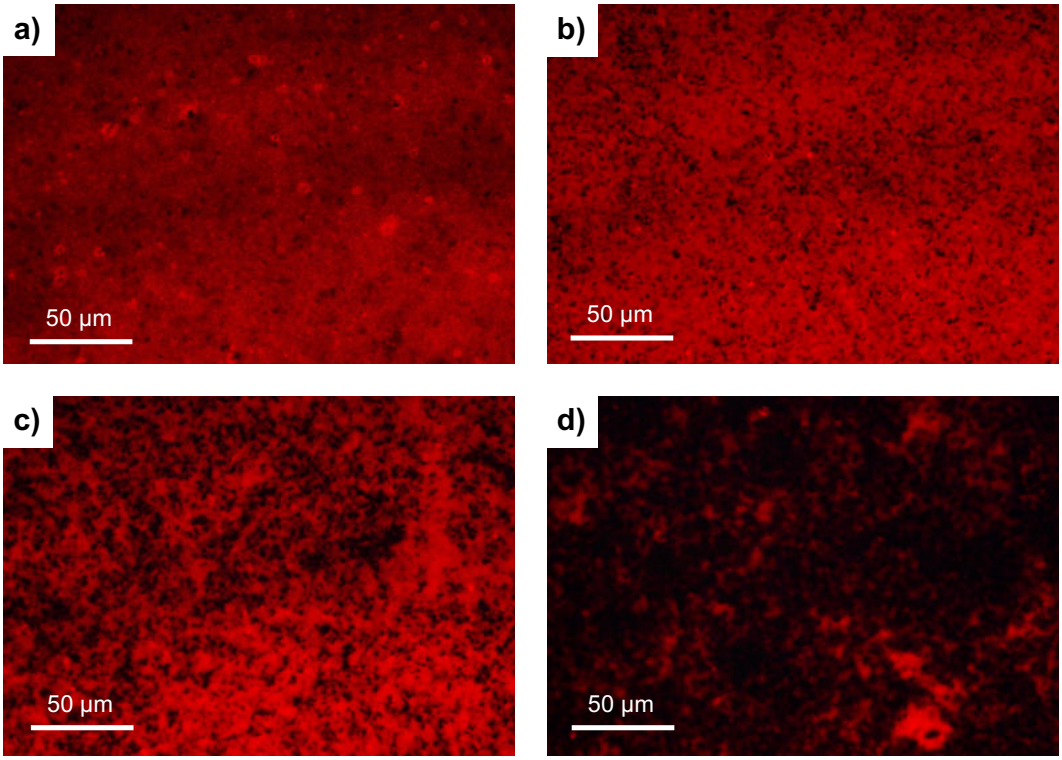

Figure 12: Microscopic image of $MAPbBrI_2$ thin films annealed at 120 °C for **a)** 0.2, **b)** 5, **c)** 10, and **d)** 30 minutes. All images were taken using a fluorescence filter at 40x magnification with an exposure time of 4 seconds.

As can be seen in **Figure 12a**, after a short annealing time to induce the colour change, multiple spots are visible, which appear to be brighter with a higher luminescence than the surrounding material. These spots are noticeably less numerous when annealing the thin films for a slightly longer time, as depicted in **Figure 12b**. The composition and the brightness of the film seem to be more homogeneous, with less colour deviation or individual spots. However, black spots without any fluorescent material considerably increase in number and size at progressively longer annealing times, as shown in **Figure 12c** and **d**.

These observations suggest that some less stable, less fluorescent material is removed from the thin films at a longer annealing time, resulting in a film with a higher PLQY. This assumption is further supported by the appearance of the thin film samples, as depicted in **Figure 13**.

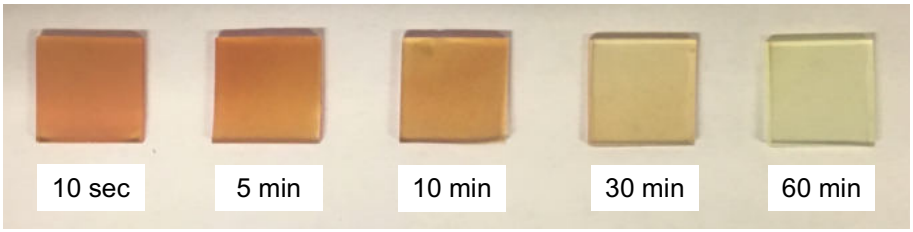

Figure 13: Picture of $MAPbBrI_2$ thin film samples, with progressively longer annealing time.

As can be seen in **Figure 13**, the decrease in colour of the thin films with increasing annealing time indicates the degradation of perovskite material. Additionally, the shift in emission maximum suggests a growth of the nanoparticles post-synthesis upon the exposure to heat or even a change in coordination between the two halides.

Multiple experiments performed on PNPs produced with the described ligand system suggest the presence of a matrix material that encapsulates the nanoparticles[43,63]. This matrix material is assumed to cause the intense agglomeration of the particles in solution while ensuring the outstanding stability of the thin film samples under ambient conditions. Additionally, as the matrix material fully encompasses the perovskite structure, it shields the core from the feasibility of changing the composition after the particle has formed, which would be needed to produce nanoparticles using anion exchange. The material removed during the annealing process is, in all likelihood excess, nonfluorescent matrix material, thus increasing the PLQY and shifting the emission maximum to slightly higher wavelengths. Furthermore, as of yet no indication has been found that an increase in annealing time would decrease the stability of the samples.

However, due to the optical microscope only displaying wavelengths visible to the human eye, the black spots found when observing the samples may be strongly emitting in the infrared range. Thus, this emission would not be visible in the images. However, no such emission is visible in the corresponding spectra, supporting the assumption of degrading material.

3.2.3. Influence of Stirring Time during Precipitation

To optimise the synthesis for mixed halide PNPs, the precipitation time was considered as well. After injecting the precursor solution into the chilled toluene, the stirring time was varied from 2 to 30 minutes. The results are depicted in **Table 5**.

Table 5: Spectroscopic properties of $MAPbBrI_2$ samples with varying stirring times during precipitation.

***t* / min**	***PLQY* / %**	**λ_{max} / nm**	***FWHM* / nm**
2	40	668	41
5	39	674	40
15	35	677	42
30	37	673	41

As shown in **Table 5**, no significant difference in PLQY values can be found in dependence on the stirring time. However, the samples differed quite visibly in optical appearance. While after 2 minutes of stirring time, a uniform, transparent film was formed, after 30 minutes, an optically thicker, less transparent film was received. To minimise the probability of self-absorption and the ensuing non-radiative recombination, a thinner sample is favourable to maximise the PLQY value. Therefore, a shorter stirring time would be beneficial while also less

time-consuming and thus, cost-effective.

However, with increasing stirring time, the emission maximum increases as well, indicating the continued growth of the nanoparticles. At 30 minutes of stirring time, the energetically lowest emission maximum of all investigated samples is reached, at 1.83 eV, amounting to a total shift of 9 nm (25 meV). As a high wavelength at high PLQY is desirable, no clear decision can be made regarding the ideal stirring time.

In order to investigate this effect and to characterise the samples further, microscopic images at 5x magnification using dark field mode and an external UV source have been taken. The resulting images can be seen in **Figure 14**.

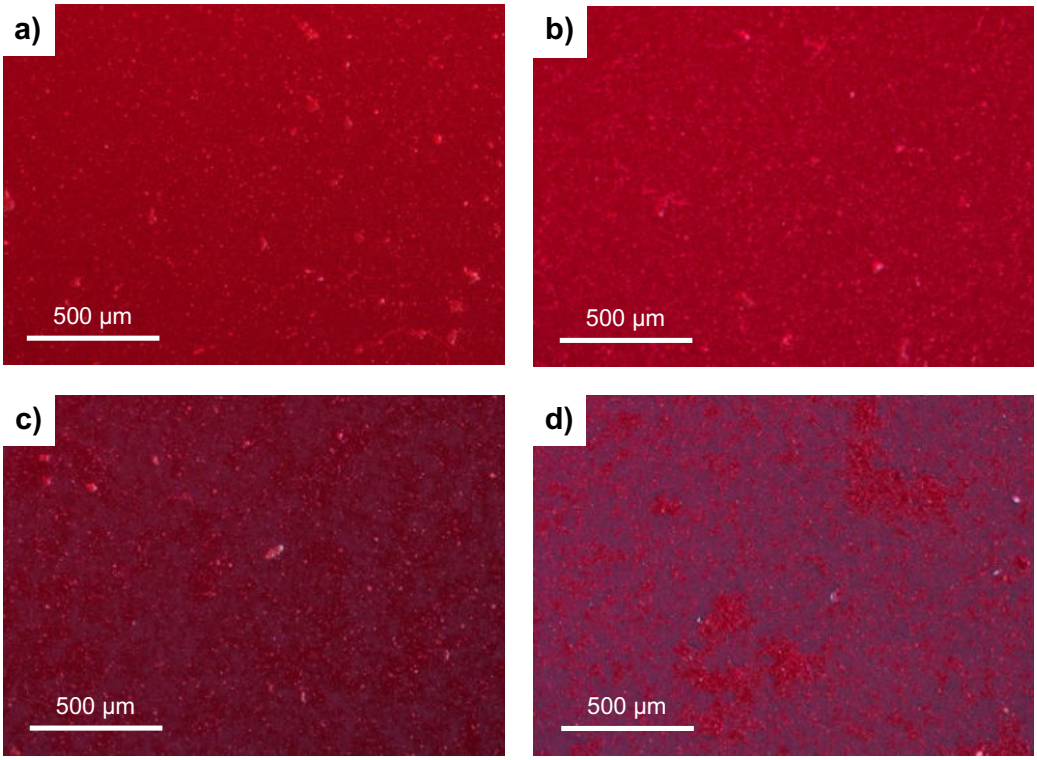

Figure 14: Microscopic image of $MAPbBrI_2$ thin films with increasing precipitation time of **a)** 2 min, **b)** 5 min, **c)** 15 min, and **d)** 30 min, showing progressive agglomeration.

As shown in **Figure 14a**, after a short stirring time of 2 minutes, a mostly uniform film is formed, displaying occasional bright spots of agglomeration. As can be seen in **Figure 14b**, upon increasing the duration of precipitation, the agglomerates noticeably increase in number. When further increasing the precipitation time, intense cluster formation is visible, where after 30 minutes, such intense clustering occurs that the glass slide becomes visible, as is seen in **Figure 14c** and **d**. This cluster formation, responsible for the decrease in absorbance, is even visible to the naked eye when observing the thin film samples. As a homogeneous film is preferable over the formation of clusters, a stirring time of 2 minutes was adapted for the general synthesis.

3.2.4. Water dependence of PNPs

Water is of significant importance during the synthesis of any type of perovskite material, as it can fully dissolve most perovskite structures, and even ambient humidity has adverse effects on the durability of the materials. Higher humidity levels revert the ABX_3 structure into its original components of AX and BX_2 salts. Even small degrees of degradation fundamentally change the behaviour of the materials[64]. With higher levels of humidity, a catalytic degradation effect is observed, culminating in the failing of perovskite-based devices[65].

However, small amounts of water are known to have a beneficial effect on the perovskite structure, as they mobilise alkylammonium salts, leading to a removal of excess cations and thus a decrease in trap states[22,66,67]. Furthermore, uncoordinated sites may be improved upon by the presence of water as well. Hydrogen bonds are formed with these sites, decreasing the possibility of a nonradiative decay and increasing the PLQY of perovskites[68].

To exclude any water contamination, anhydrous solvents were employed during the synthesis. Molar equivalents of water with respect to the amount of PbX_2 in the nanoparticles were added to the precursor solution to study the effect of water, as depicted in **Figure 15**.

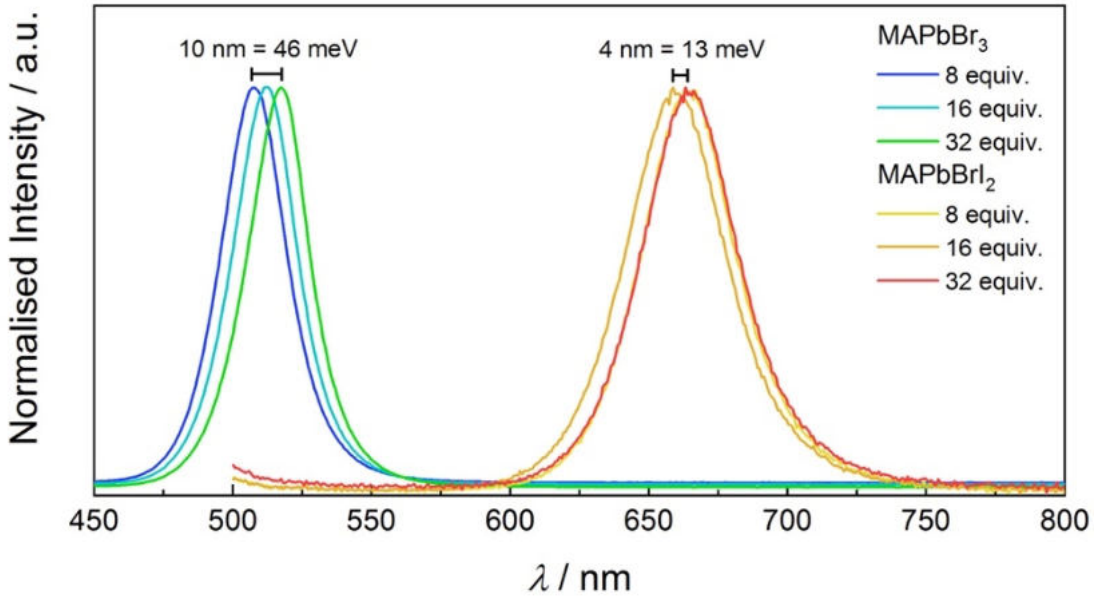

Figure 15: Photoluminescence spectra of $MAPbBr_3$ and $MAPbBrI_2$ nanoparticles with an increasing volume of water added to the precursor (from 8 to 32 equiv.).

As shown in **Figure 15**, increasing the water content of the precursor has a linear effect on the emission maximum of $MAPbBr_3$ PNPs. Upon doubling the amount of water from 8 to 16 and then further to 32 equiv., the emission successively shifts to higher wavelengths. In contrast, no continuous shift can be seen in mixed halide nanoparticles when increasing the water content from 8 up to 32 equiv. Neither the emission maximum nor the PLQY value

showed a linear trend, with changes being within the variance of the synthesis and measurement system.

In order to investigate this phenomenon further, precursor solutions with 32 equiv. water were prepared. An additional amount of water was added to the precursor prior to the injection into the chilled toluene. The results for fully bromide $MAPbBr_3$ nanoparticles are depicted in **Figure 16**.

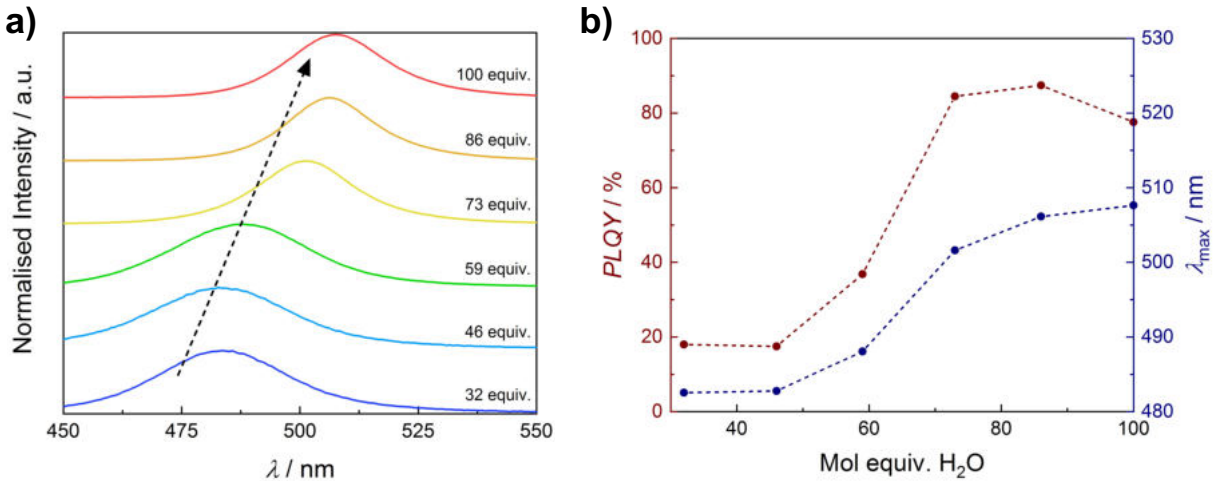

Figure 16: a) Photoluminescence spectra of $MAPbBr_3$ nanoparticles with increasing amounts of water added during the precipitation as well as **b)** development of PLQY and emission maxima in dependence on the amount of water.

As can be seen in **Figure 16a**, the emission maximum is continuously bathochromically shifted with increasing water concentration, amounting to a total shift of 25 nm (126 meV). However, when looking at the trend of PLQY depicted in **Figure 16b**, it can be seen that a maximum is reached at 86 mol equiv. Above this value, the PLQY decreases, indicating an excess of water starting to degrade the perovskite structure and facilitating the formation of trap states through vacancies, thus reducing the probability of radiative recombination.

Interestingly, and in contrast to the fully bromide particles, mixed halide PNP of the composition $MAPbBrI_2$ did not show a drastic shift upon the addition of water. A comparison of the two different compositions can be seen in **Figure 17**.

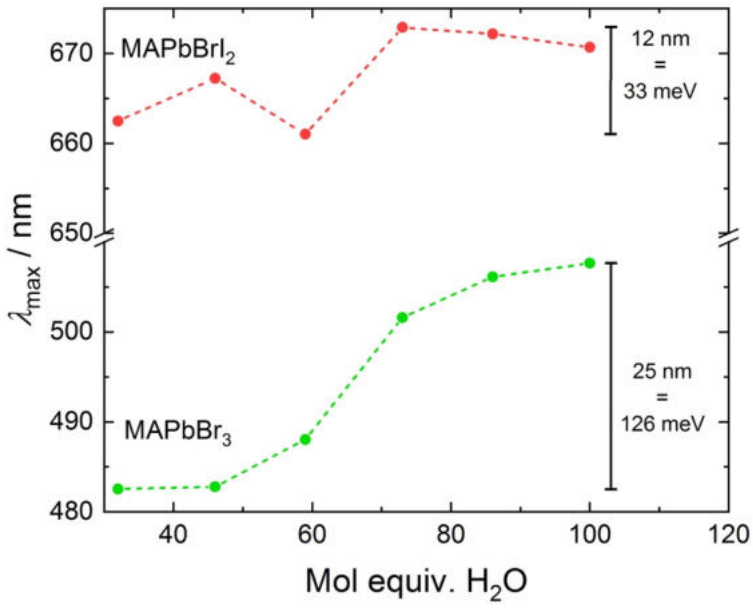

Figure 17: Comparison of the emission maxima of $MAPbBr_3$ (green line) and $MAPbBrI_2$ (red line) in dependence on the amount of water added during the precipitation.

As can be seen, while the emission maximum of $MAPbBr_3$ increases steadily, no clear trend is found for the mixed halide $MAPbBrI_2$ particles. The change in 12 nm (33 meV) can be explained by ordinary fluctuation during the synthesis with no dependence upon the introduction of water visible. Furthermore, while the quantum yield of the fully bromide PNPs increased 4.8-fold (from PLQY values of 18 % to 87 %), the mixed halide particles merely increased 1.3-fold (from 28 % to 37 %). Hence, the thus produced mixed halide PNPs appear to be remarkably tolerant to the presence of water. Exclusion of humidity during the synthesis does not seem necessary, nor is it essential to use anhydrous solvents.

The effects of water on perovskite materials are well documented, as even minuscule amounts such as gaseous water molecules found in the atmosphere may influence the hydrogen bonds between the PbX_6^{3-} octahedra and the cations occupying the formed void[69]. Furthermore, the fluorescent properties of perovskites are so sensitive to the presence of water that $CsCuBr_3$ is even proposed as a sensor for water contamination of anhydrous DMF[70]. Considering these reports, the tolerance of the prepared $MAPbBrI_2$ towards water is genuinely remarkable and promising.

3.2.5. Ageing of Precursor

To characterise the stability of the precursor solution, nanoparticles were precipitated over a period of up to six days after the manufacture of the precursor solutions. The development of the photoluminescence spectra of four different compositions of PNPs throughout this period is depicted in **Figure 18** below.

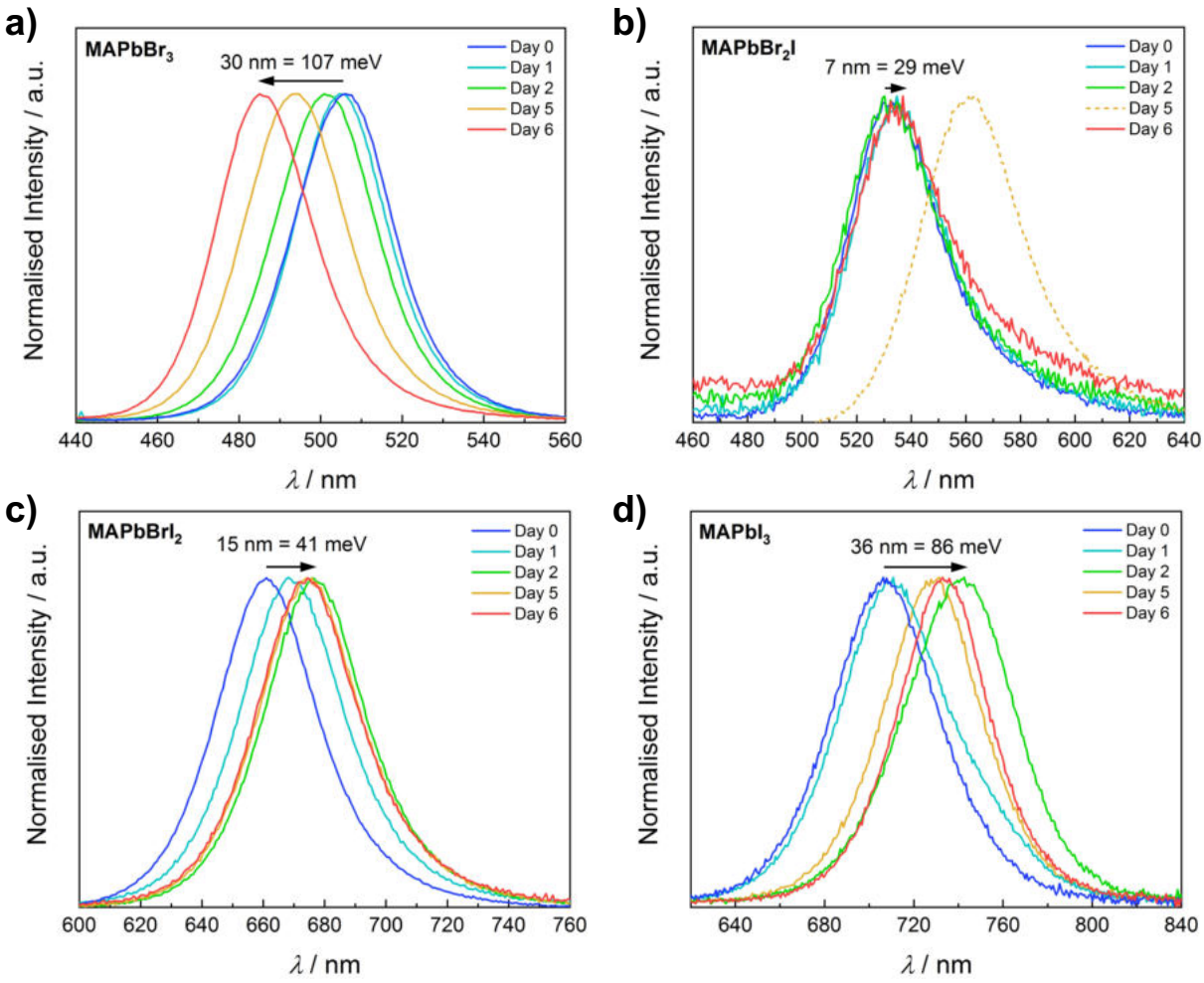

Figure 18: Change in photoluminescence spectra with successive ageing of a precursor of **a)** $MAPbBr_3$, **b)** $MAPbBr_2I$, **c)** $MAPbBrI_2$, and **d)** $MAPbI_3$ thin films.

As shown in **Figure 18a**, when precipitating $MAPbBr_3$ nanoparticles after several days of stirring, a hypsochromic shift to an energetically higher emission can be seen. After the precursor solution had aged for six days, a maximum shift of 30 nm (107 meV) to lower wavelengths was observed. Interestingly, this trend reverses upon introducing iodide to the crystal lattice. As can be seen in **Figure 18b**, a slight bathochromic shift is already visible at low iodide concentrations. After five days of stirring the precursor solution, a significant and sudden shift of 33 nm (137 meV) can be seen. However, as the emission maximum reverts close to the initial value after six days, the $MAPbBr_2I$ sample prepared on day five has been deemed an outlier and excluded from any further consideration.

The magnitude of the bathochromic shift increases with rising iodide content. While PNPs at low iodide content hardly shift in emission maximum with ageing precursor, nanoparticles with a majority of iodide compared to bromide in the crystal lattice show a substantial shift in emission maximum. Perovskites of the composition $MAPbBrI_2$, with 33 % iodide content show an increase in emission wavelength of 15 nm (41 meV), as can be seen in **Figure 18c**, while nanoparticles of the composition $MAPbI_3$ show an increase of 36 nm (86 meV), which is

depicted in **Figure 18d**.

A shift in emission maximum of PNPs is most likely the result of a change in the size of the nanoparticles, as the impact of the quantum confinement effect is increased or decreased[6,9,22,51]. Apart from a simple growth of the particles, a difference in composition for mixed halide particles may also cause the shift in emission, as iodide is much more spatially demanding than bromide and decreases the band gap energy. However, this does not explain the prominent and adverse shifts of the pure halide particles $MAPbBr_3$ and $MAPbI_3$. It seems that bromide particles decrease in size upon longer stirring of the precursor solution. This might be due to the fact that the ligands stabilise the surface more effectively, resulting in stronger quantum confinement and a higher energy emission. The reverse is occurring for fully iodide particles, as those seem to increase in size upon longer stirring. This adverse effect may result from the difference in complexation tendency of the different halides with the lead centre. However, further studies would have to be carried out to prove this hypothesis adequately.

Furthermore, the trend of PLQY with increasing precursor age was studied as well. The results for varying compositions of PNPs are depicted in **Figure 19**.

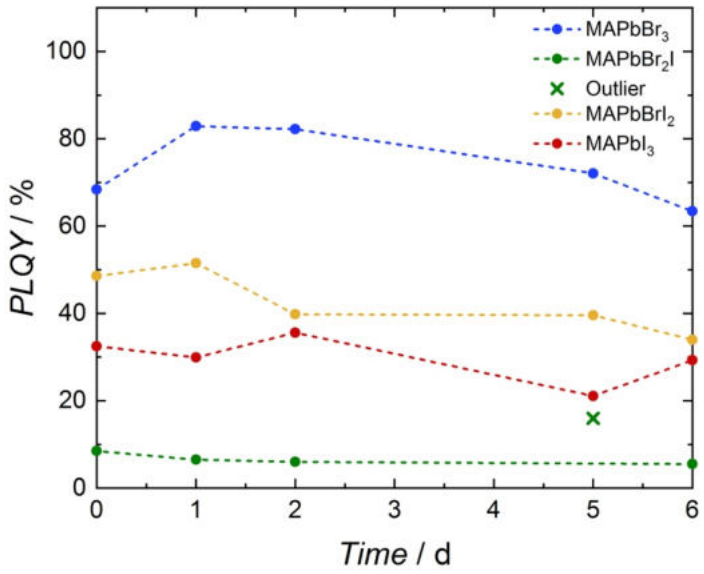

Figure 19: Development of PLQY values of PNPs made from varying compositions with successive ageing of the precursor solution as well as a marked outlier of the $MAPbBr_2I$ thin film sample.

As shown in **Figure 19**, all compositions of PNPs exhibit the highest PLQY values within the first two days, as the values decrease over time. Overall, $MAPbBr_2I$ nanoparticles display the lowest values, decaying from 8.5 % to successively smaller values. A reasonably high value was only achieved after a stirring time of the precursor solution for five days however, this sample, marked in **Figure 19**, was deemed to be an outlier as both the PLQY as well as the emission maximum fall outside the range of all other samples prepared of the same composition.

A stirring time of one day for all other compositions produced reasonably satisfying results and was therefore adopted in the standard synthesis.

3.3. Photoluminescence Quantum Yield and Emission Maximum

To compare the PLQY and emission maximum, a box plot was compiled of samples prepared according to the general synthesis. The median, the extreme values as well as the outliers are also displayed in the box plot, as can be seen in **Figure 20**.

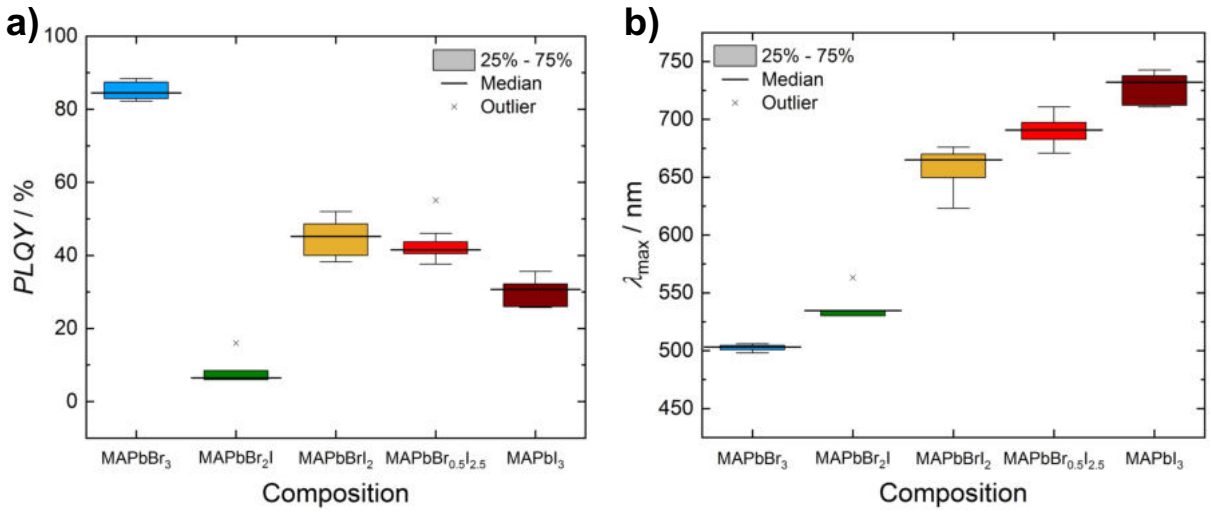

Figure 20: Comparison of **a)** mean PLQY and **b)** emission maxima of perovskite nanoparticles with varying halide composition.

When comparing the PLQY values of the various compositions depicted in **Figure 20a**, it is immediately evident that the fully bromide particles display the highest value by far, at a median value of 85 %. However, surprisingly, upon introducing small contents of iodide (33 %), the PLQY value drops off tremendously to a median value of 7 %.

For mainly iodide PNPs, the overall best composition in terms of PLQY was found to be $MAPbBrI_2$, at a median value of 45 %. A minor increase of iodide content to a composition of $MAPbBr_{0.5}I_{2.5}$ slightly lowered the median PLQY value to 41 %, while fully iodide PNPs yielded a value of 31 %. The overall highest value of 55.1 % was reached at a composition of $MAPbBr_{0.5}I_{2.5}$ (roughly 83 % iodide content).

When comparing the mean emission maxima of the different compositions, as depicted in **Figure 20b**, it is found that the scattering of the values increases with increasing iodide content, with a broader range of emission maxima found across various samples. The emission maximum increases with rising iodide content, with a jump occurring between majority bromide and majority iodide halide composition. Though particles emitting in the relevant region between 550 and 650 nm were synthesised, no PLQY values above 10 % were achievable. As it was not the main focus of this thesis, optimisation of the synthesis was omitted, and

$MAPbBr_2I$ was chosen as a reference composition, despite the low quantum yield.

In terms of stability, $MAPbBr_3$ thin film samples prepared with *t*boc-lysine and hexanoic acid are already known to possess extremely high stability, with PLQY losses lower than 5 % over the first 30 days[56]. Similar values have been found for iodide rich PNP thin film samples, as a PLQY decay of 5 % ± 2.5 % was found for samples prepared according to the general synthesis over the first 30 days while being stored at ambient conditions. These values are truly remarkable, as stability in thin film samples is rarely achieved in PNPs, often decaying within days after fabrication[19,38,41].

3.4. Photoluminescence Excitation

Perovskite materials are known for their large absorption coefficient and broad absorption over the whole visible spectrum. Photoluminescence excitation spectra have been recorded for PNPs with varying contents of iodide. The results are depicted in **Figure 21** below.

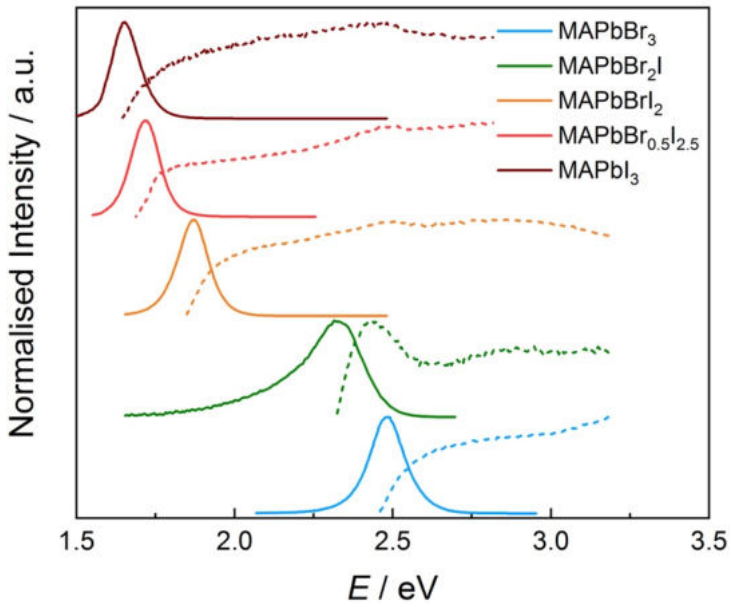

Figure 21: Normalised photoluminescence emission (solid line) and photoluminescence excitation spectra (dashed line) of nanoparticles with varying iodide content. The excitation wavelength was set to 405 nm for bromide rich particles and 475 nm for iodide rich particles. Detection wavelengths for photoluminescence excitation spectroscopy were set to 510 ($MAPbBr_3$), 545 ($MAPbBr_2I$), 680 ($MAPbBrI_2$), 740 ($MAPbBr_{0.5}I_{2.5}$) and 760 nm ($MAPbI_3$).

As shown in **Figure 21**, most samples depict a broad absorption with a more or less defined absorption edge. However, the sample containing 33 % iodide, $MAPbBr_2I$ does not follow this behaviour, as it displays a distinct absorbance peak at 512 nm (2.42 eV) with a pronounced Stokes shift of 25 nm (86 meV), which no other sample displays as noticeably. Furthermore, the absorbance spectra of all iodide rich particles show a local maximum at roughly 494 nm (2.51 eV). This might indicate the presence of bromide rich spots within the individual films[44]. However, as this local maximum is also present in the fully iodide $MAPbI_3$ sample, a definite

conclusion as to the origin cannot be reached.

From the photoluminescence excitation spectra, Tauc plots were created to determine the optical band gap energies[71]. The relevant equation for the transformation of the y-axis is depicted in **Equation 2**.

$$(\alpha E)^{1/\gamma} = B (E - E_{og}) \quad \text{(Eq. 2)}$$

with: α = absorption coefficient

E = photon energy (E = h ν)

γ = factor describing the nature of the electron transition (½ for direct, 2 for indirect)

B = constant

E_{og} = optical band gap energy

As the absorption coefficient was not determined for thin film samples, the Tauc plot was approximated using the normalised photoluminescence excitation spectra. Since perovskites are considered to be direct band gap semiconductors, a factor of ½ was implemented in **Equation 2**[72,73]. The results can be found in **Table 6**.

Table 6: Optical band gap energies of PNP thin film samples with varying compositions.

Sample	λ_{max} **/ nm**	***PLQY* / %**	E_{og} **/ eV**
$MAPbBr_3$	498	83	2.45
$MAPbBr_2I$	536	5	2.33
$MAPbBrI_2$	662	39	2.06
$MAPbBr_{0.5}I_{2.5}$	723	31	2.03
$MAPbI_3$	750	26	1.87

As shown in **Table 6**, a maximum shift in band gap energy of 0.58 eV could be achieved upon the total substitution of bromide with iodide. This shift is comparable in magnitude to the results achieved from different synthesis methods, like anion exchange or grinding synthesis[48,74–76]. Furthermore, the band gap values for different compositions are higher than those reported for bulk materials, confirming the quantum confinement of all samples[77,78].

3.5. Low-Temperature Spectroscopy

Low-temperature spectroscopy is a powerful tool to study changes in the band gap, exciton binding energy and electronic structure of semiconductors[79]. Photoluminescent properties are mainly characterised by exciton recombination, exciton-phonon interaction, size distribution and energetic trap states. At low temperatures, thermally activated non-radiative recombination decreases in probability, allowing for the observation of other processes within the material. Furthermore, phase transitions and their impact on optical properties may be

observed, which are essential parameters for the application of PNPs in optoelectronic devices[80].

The Varshni model is an empirical model to predict the optical properties of semiconductors at a lower temperature. It states that usually, decreasing the temperature leads to a successive hypsochromic shift of the emission[81]. Perovskites do not follow this empirical model, as with decreasing temperature, a bathochromic shift is observed. The origin of this red shift is widely believed to be lattice thermal expansion. With an increase in temperature, the s orbital of Pb and the p orbital of the halide decrease their interaction as the lattice expansion reduces the overlapping of the orbitals. As these orbitals make up the valence band, the band gap energy increases, resulting in a blue shift with increasing temperatures[80,82].

Along with a shift in the emission energy, a change in the absorption has to be considered as well. As the absorbance spectrum was not measured at lower temperatures, any possible changes were estimated by comparing the PLQY at room temperature with the emission intensity in dependence on the temperature. With increasing intensity, the PLQY increases accordingly. However, as no values higher than 100 % are feasible, surpassing this value may indicate a change in the absorbance spectrum with varying temperature.

All measurements were performed between 5 and 295 K on five different samples with varying iodide content ($MAPbBr_3$ to $MAPbI_3$). Samples were analysed in terms of changes in peak shape, integrated intensity, FWHM and emission maximum.

The Arrhenius equation expresses the temperature dependent photoluminescence intensity, as depicted in **Equation 3**[83–85].

$$I(T) = \frac{I_0}{1 + A\, e^{-E_b / k\,T}} \qquad \text{(Eq. 3)}$$

with: I_0 = intensity at 0 K

A = pre-exponential coefficient

E_b = exciton binding energy

k = Boltzmann constant ($8.617 \cdot 10^{-5}$ eV K^{-1})

T = temperature

If the photoluminescence intensity decreases drastically with the temperature, a two-step quenching model may be used, as displayed in **Equation 4**[86]. In this equation, two separate processes are assumed to contribute to the photoluminescence quenching.

$$I(T) = \frac{I_0}{1 + A_2\, e^{-E_{b,1} / k\,T} + A_2\, e^{-E_{b,2} / k\,T}} \qquad \text{(Eq. 4)}$$

In general, E_b is often attributed to the thermal dissociation energy of the free exciton or the exciton binding energy. It determines whether free electron / hole pairs or predominately bound excitons generate the response upon exciting the material. However, using low-temperature spectroscopy to determine the exciton binding energy follows the assumption that only recombination of bound excitons results in luminescent emission. As this is not entirely the case, the values received from fitting temperature dependent spectroscopic data are slightly exaggerated and should be seen as characterising the upper limit of the exciton binding energy[87–90].

Furthermore, FWHM is a characteristic parameter for photoluminescence spectra as it results from different localised states emitting at the same time. The FWHM is analysed over the whole temperature range, and the temperature dependence is studied with the Boson model, as depicted in **Equation 5**[84,86].

$$\Gamma(T) = \Gamma_0 + \sigma T + \frac{\Gamma_{op}}{e^{E_{ph}/kT} - 1} \qquad \text{(Eq. 5)}$$

with: Γ_0 = inhomogeneous broadening

σ = exciton-acoustic phonon interaction

T = temperature

Γ_{op} = exciton-optical phonon contribution to line width broadening

E_{ph} = average phonon energy participating in quenching process

k = Boltzmann constant ($8.617 \cdot 10^{-5}$ eV K^{-1})

In **Equation 5**, the first term characterises inhomogeneous broadening, especially at low temperatures, while the second and third terms contribute to homogeneous broadening. The second term describes the contribution of exciton-acoustic phonon coupling to the line width, while the third term characterises the interaction of excitons with longitudinal optical phonons. A fourth term can be used to express homogeneous line broadening due to trap states and impurities however, as perovskite materials are low in trap states, especially deep traps, this term has been omitted in this work[91].

3.5.1. $MAPbBr_3$

The results of the low-temperature spectroscopic measurements of $MAPbBr_3$ are depicted in **Figure 22**. As shown in **Figure 22a**, a fully symmetric, Gaussian emission peak is present at room temperature, while at lower temperatures, an asymmetric peak shape, with broadening at the higher energy side is visible. When observing the spectrum, a total hypsochromic shift of 19 nm (89 meV) is seen with increasing temperature, from 2.32 eV at 5 K to 2.41 eV at 295 K.

To properly fit the spectrum, two individual Gaussian peaks have been used at lower temperatures up to 170 K, with the lower energy one labelled peak 1 and the energetically higher one labelled peak 2. At temperatures higher than 170 K, peak 1 disappears with only peak 2 contributing to the spectrum. Thus, only peak 2 has been considered for calculations concerning FWHM and emission maximum.

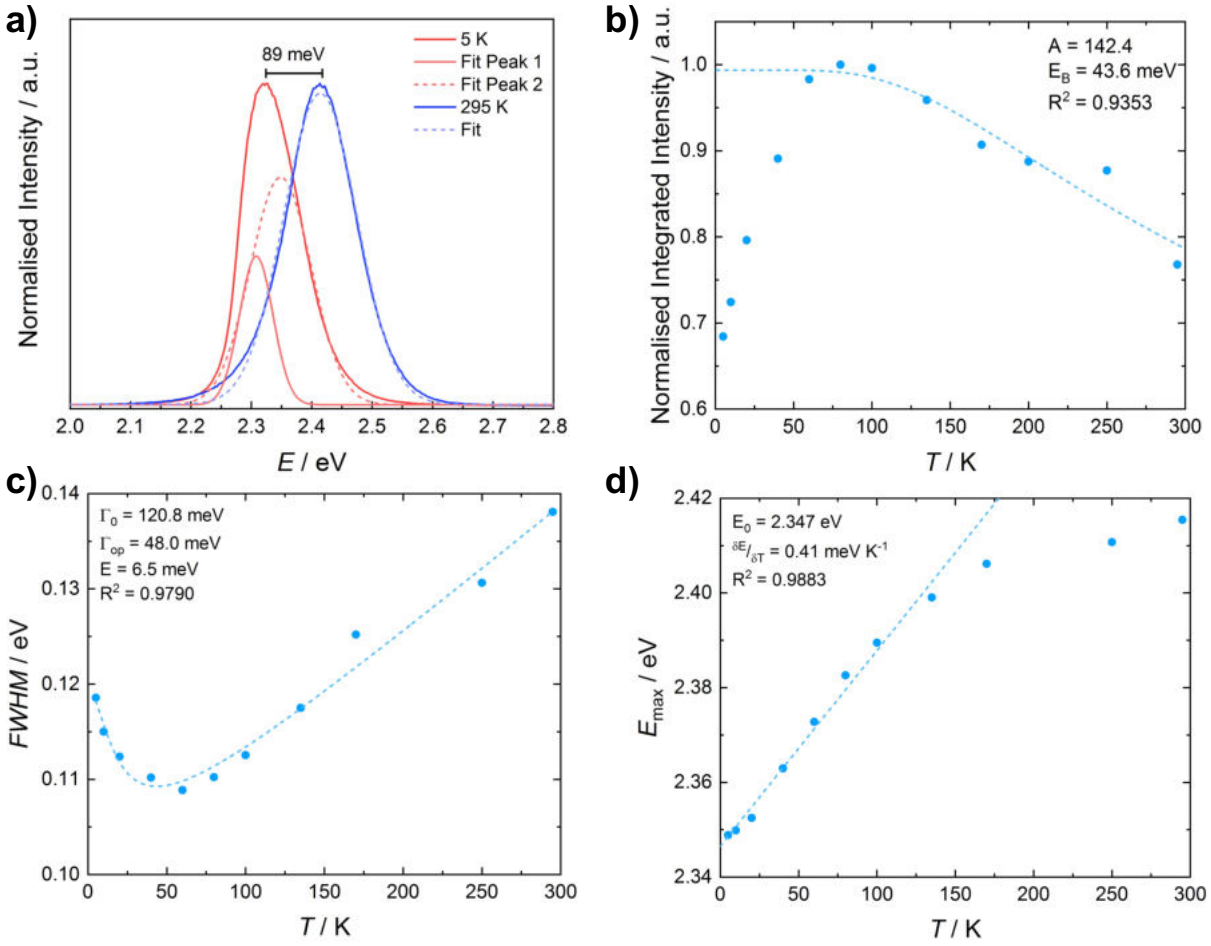

Figure 22: Results of the low-temperature spectroscopic measurements of a $MAPbBr_3$ thin film sample. **a)** Normalised photoluminescence spectra at 5 K (red line) and 295 K (blue line) with Gaussian fit, highlighting the presence of two peaks at lower temperatures, **b)** normalised integrated intensity as a function of temperature, **c)** full-width at half maximum of peak 2 as a function of temperature and **d)** emission maximum of peak 2 as a function of temperature with linear fit characterising the increase of emission maximum at low temperatures.

As can be seen in **Figure 22b**, the emission intensity rises with increasing temperature up to a maximum at 80 K. After this point, the emission intensity steadily decreases until reaching room temperature. **Equation 3** has been used to fit the emission intensity in dependence of the temperature for all values above 60 K, as a steady state at the origin is required to receive meaningful results. An exciton binding energy of 44 meV was found from the data, which is slightly larger than the values measured for bulk materials due to the influence of quantum confinement on nanosized particles[92,93].

The anomaly in emission intensity with a maximum at 80 K has been seen before in nanoparticles, for example, in thiol capped PbS[94] quantum dots, silicon quantum dots[95] and quantum confined perovskite nanoparticles[96]. Previous reports have attributed the initial rise in emission intensity to carriers confined in trap states overcoming shallow energy barriers using thermal energy, falling into the ground state and contributing to the overall emission. However, nonradiative recombination increases after surpassing a certain threshold temperature, and the intensity steadily decreases until reaching room temperature. This anomaly was found for all samples discussed in this work.

Figure 22c displays the FWHM as a function of temperature. Initially, as the temperature rises, the FWHM decreases until a threshold temperature of 60 K is reached, at which the trend reverses, and line broadening occurs. This threshold temperature is around the same temperature as the reversal of the trend in intensity against temperature, as has already been discussed in **Figure 22b**. Previous reports have attributed this non-monotonous behaviour to a phase transition between the room temperature stable tetragonal phase and the low temperature stable orthorhombic phase. Model calculations state smaller band gap energies for the orthorhombic phase, which coincides with the hypsochromic shift upon decreasing the temperature[84]. Furthermore, a shift in phases would support the observation of the evolution of a second peak at low temperatures. This evolution of the second peak at 170 K coincides well with literature reports, where phase coexistence occurs between 140 and 170 K for various compositions[97–101]. Due to this nonlinear peak broadening, a large contribution of inhomogeneous line broadening to FWHM was found at 121 meV, with the linear contribution due to optical phonon interaction only being 48 meV.

When observing the shift in emission maximum in dependence on the temperature, a continuous hypsochromic shift with increasing temperature can be seen. However, the emission does not change linearly, as shown in **Figure 22d**. While the emission changes more rapidly at lower temperatures, after 150 K the magnitude of the shift decreases. At lower temperatures, the emission maximum decreases at a rate of 0.41 meV K^{-1} until an extrapolated emission maximum of 2.35 eV (528 nm) at 0 K is reached, amounting to a total shift of 19 nm (89 meV) over the observed temperature range.

3.5.2. $MAPbBr_2I$

A bromide rich mixed halide $MAPbBr_2I$ thin film sample has also been investigated using low-temperature spectroscopy, with the results depicted in **Figure 23**. Both the spectrum at 5 K and the spectrum at 295 K display a large tail on the lower energy side of the spectrum, decreasing in intensity as the temperature decreases, as shown in **Figure 23a**. As all spectra at any temperature are deconvoluted with two individual Gauss curves, only the higher energy

peak was used in the data analysis, while the broader lower energy peak characterising the tail was omitted from data fitting. However, both the trends for FWHM as well as emission maximum in dependence on the temperature show identical behaviour for either peak.

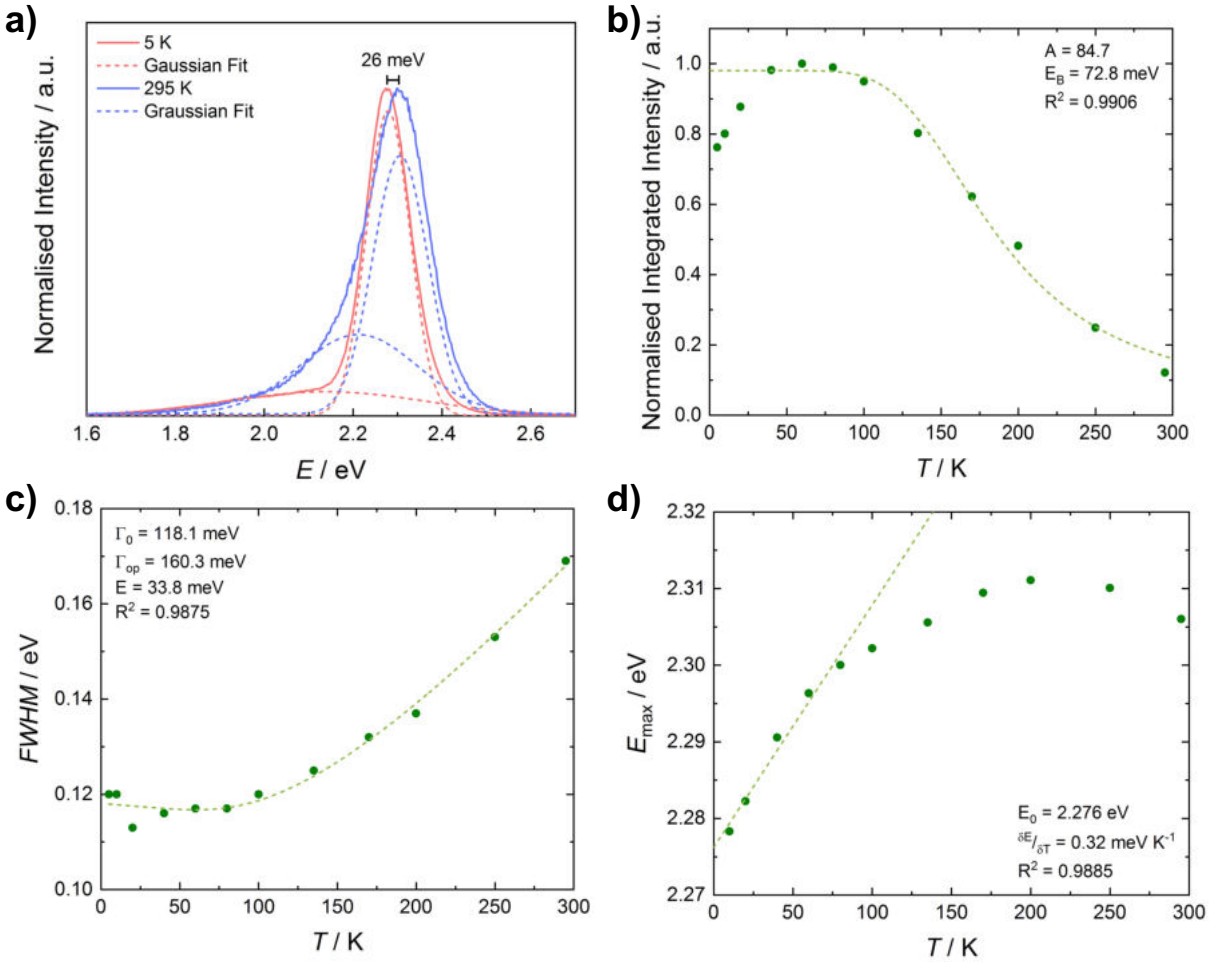

Figure 23: Results of the low-temperature spectroscopy of a $MAPbBr_2I$ thin film. **a)** Photoluminescence spectra at 5 K (red) and 295 K (blue) along with the fit of two individual Gauss curves (dashed line), **b)** normalised integrated intensity as a function of temperature, **c)** FWHM of the higher energy peak as a function of temperature, as well as **d)** shift in emission maximum as a function of temperature with a linear fit for the lower temperature region.

When fitting the normalised integrated photoluminescence intensity as a function of the temperature using **Equation 3**, an exciton binding energy of 73 meV is obtained, as shown in **Figure 23b**. It must be stated that only the values up to the maximum at 50 K were used to fit the data. Most reports state that the exciton binding energy of perovskite nanoparticles is between 60 and 10 meV. Furthermore, with an increasing atomic number of the halogen, the exciton binding energy decreases[92,93,102]. However, substantially larger exciton binding energies in the range of 150 - 300 meV have also been reported[103,104], as has the opposite trend of rising exciton binding energy with increasing iodide content[96,100]. As exciton characteristics of perovskite nanoparticles are primarily dependent on the type of synthesis and the specific conditions at which the particles are synthesised, differences in trends and

magnitude are well reported in literature[100].

The shift in FWHM in dependence on the temperature follows the expected trend, with only a slight deviation at low temperatures, as can be seen in **Figure 23c**. After fitting the received data, an inhomogeneous peak broadening of 118 meV was found, while the optical phonon interaction amounted to 160 meV.

A hypsochromic shift with increasing temperature is observed in **Figure 23d**, which is typical for perovskite type semiconductors. However, this shift does not occur entirely continuously, as a maximum is found at 200 K, after which the emission maximum decreases again in energy. Furthermore, the magnitude of the peak shift is higher at lower temperatures, with a shift of 0.32 meV K^{-1}, while the maximum energy increases at a lower rate after passing 80 K. Using the lower part of the data, an emission maximum of 545 nm (2.28 eV) was found for 0 K. Over the whole temperature range a total shift of 6.2 nm (26 meV) was observed, which is substantially less than is found in purely bromide films.

3.5.3. $MAPbBrI_2$

A mixed halide PNP sample of the composition $MAPbBrI_2$ has also been analysed at low temperatures, with the results depicted in **Figure 24**. As shown in **Figure 24a**, the fluorescence spectrum at room temperature shows a fully Gaussian distribution. However, at 170 K, a shoulder develops on the higher energy side of the spectrum, which is deconvoluted into two separate peaks. The lower energy peak is already visible at room temperature, while the higher energy peak starts to develop at low temperatures continuing down to 5 K. As previously discussed, this indicates a high temperature stable tetragonal phase and a low temperature stable orthorhombic phase. In this sample, phase coexistence is present over the whole range from 170 K downwards. However, the tetragonal phase stays the dominant state, accounting for 54 % at 5 K.

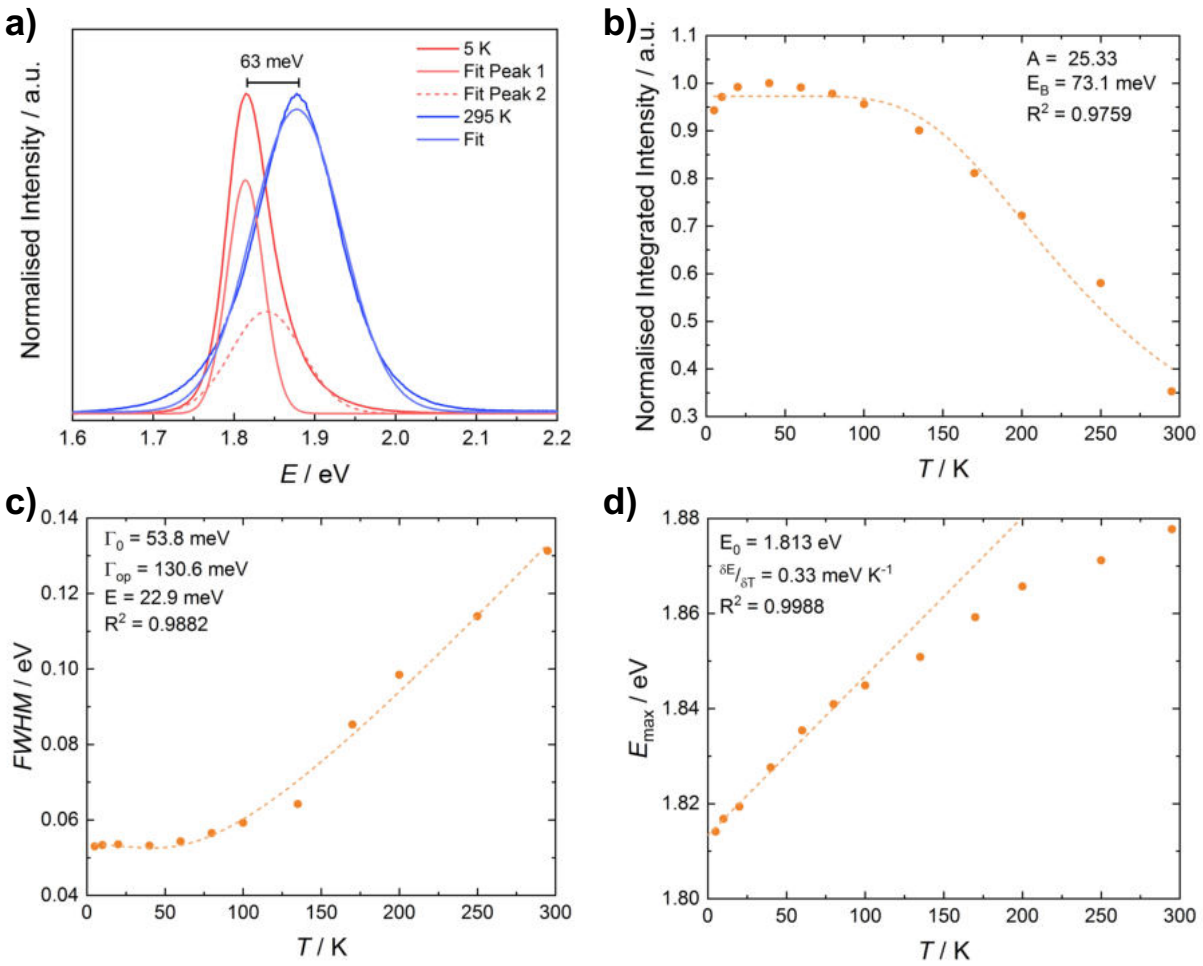

Figure 24: Results of the temperature dependent measurements of an iodide rich $MAPbBrI_2$ thin film sample. **a)** Difference in emission spectra at 5 K (red) and 295 K (blue), as well as Gaussian fit of spectra showing the evolution of an energetically higher peak at low temperatures, **b)** normalised integrated intensity as a function of temperature, **c)** FWHM of the energetically lower peak as a function of the temperature as well as **d)** shift of emission maximum as a function of temperature over the observed temperature range.

The change of the normalised integrated intensity over the temperature shows near perfect behaviour, as it decreases steadily over time, with a maximum at 40 K and a slight decrease thereafter. Thus, the whole range was used to analyse the data according to **Equation 3**, with the fit depicted in **Figure 24b**. An exciton binding energy of 73 meV was received, which is almost identical to the value found for the bromide rich mixed halide composition, depicted in **Figure 23b**. However, adjusting the PLQY value at room temperature for the increase in emission intensity, a value of 114% is found at 40 K. This indicates that along with the emission maximum, the absorption shifts as well with decreasing temperature. Thus, all values received from the fitting of this sample have to be considered accordingly.

The trend of peak broadening with increasing temperature has been studied and can be seen in **Figure 24c**. Given that the energetically lower peak is present over the whole temperature range, only this peak has been used for the analysis. However, at the temperature range where

the higher energy peak is present, it follows the same trend as the energetically lower peak. According to **Equation 5**, an inhomogeneous contribution of 54 meV was found when fitting the lower energy peak, with an exciton phonon interaction of 131 meV.

The emission maximum over the temperature range develops nearly linearly, as can be seen in **Figure 24d**, with a slight decrease in rate occurring at temperatures higher than 100 K, consistent with the phase change from tetragonal to orthorhombic. At lower energies, the emission maximum changes at a rate of 0.33 meV K^{-1}, concluding with a projected emission maximum of 1.81 eV at 0 K.

A second iodide rich PNP sample of the composition $MAPbBr_{0.5}I_{2.5}$ was analysed at low temperatures as well, with the resulting spectra depicted in **Figure 25**.

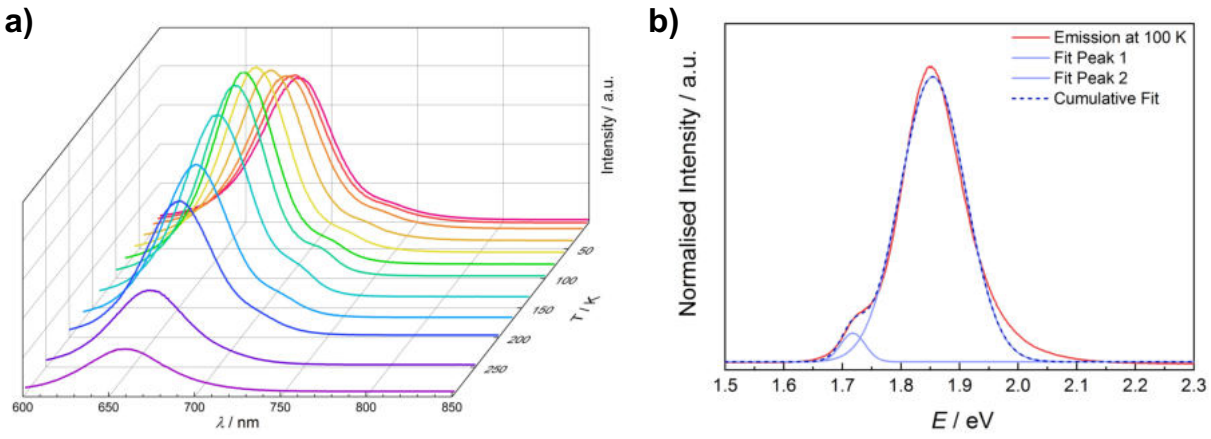

Figure 25: a) 3D photoluminescence spectra in dependence of the temperature of a $MAPbBr_{0.5}I_{2.5}$ thin film sample along with **b)** spectrum at 100 K (red) with two individual Gauss curves for peak deconvolution (light blue) and cumulative spectrum (blue dashed).

As can be seen in **Figure 25a**, this sample develops a very noticeable shoulder at the lower energy side of the spectrum starting at 170 K. The spectrum is deconvoluted using two Gauss curves, revealing a low intensity peak at lower energies and a higher intensity peak at higher energies, as can be seen in **Figure 25b**. However, no fit was achieved when analysing the FWHM of either peak as a function of the temperature. According to **Equation 3**, an exciton binding energy of 92 meV was reached when analysing the intensity in dependence on the temperature, following the trend of increasing energy with increasing iodide content.

3.5.4. $MAPbI_3$

Furthermore, a fully iodide $MAPbI_3$ thin film sample has been characterised using low-temperature spectroscopy, as is depicted in **Figure 26**. In contrast to all other samples studied in this work, $MAPbI_3$ does not show any peak distortion at lower temperatures. As can be seen in **Figure 26a**, even at 5 K, the peak shape stays symmetric and can be described by one single Gauss curve, at an almost identical coefficient of determination as the spectrum at 295 K. A slight peak distortion can be seen from 135 to 170 K however, it is not large enough

to be successfully fitted with two curves. In total, the emission shows a hypsochromic shift with increasing temperature at a magnitude of 16 nm (33 meV) from 5 to 295 K.

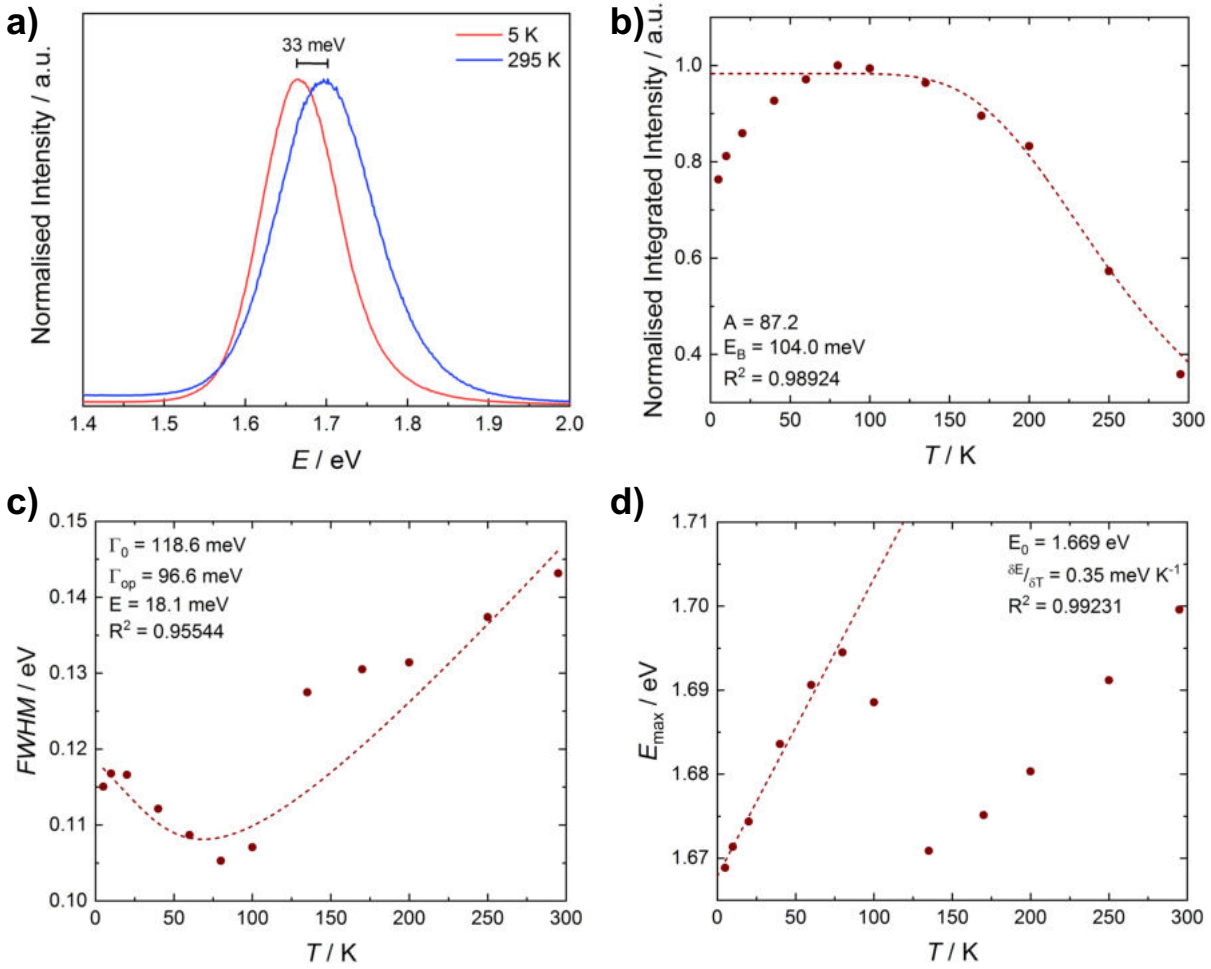

Figure 26: Results of temperature dependent spectroscopic measurements of a fully iodide $MAPbI_3$ thin film sample. **a)** Difference in the emission spectrum between 5 K (red) and 295 K (blue), **b)** integrated intensity as a function of the temperature, showing an abnormal maximum at 80 K, **c)** FWHM as a function of the temperature as well as **d)** emission maximum as a function of the temperature showing a highly irregular trend.

As shown in **Figure 26b**, the peak intensity rises with increasing temperature until a threshold is reached at 80 K. Surpassing this point, the intensity decreases with increasing temperature. Similar behaviour is found with samples of different halide compositions. Thin films of fully bromide and bromide rich PNPs likewise show a maximum at 80 K, attributed to a phase transition from tetragonal to orthorhombic phase. When fitting the data, an exciton binding energy of 104 meV was found, which fits with the observed trend of increasing energy with increasing iodide content.

When plotting FWHM as a function of the temperature, as is seen in **Figure 26c**, the same trend is found as with previous samples, where initially the line width decreases with temperature until a threshold of 80 K, where it then increases. To fit the data according to **Equation 5**, the values at 135 K and 170 K were excluded. Thus, an inhomogeneous

contribution of 119 meV was found, with an optical phonon coupling of 97 meV.

However, when observing the development of the emission maximum with temperature, an extremely inhomogeneous behaviour is found, with turning points at 80 and 135 K, as shown in **Figure 26d**. The same behaviour has been seen in $MAPbI_3$ samples before and attributed to a phase change from the low temperature stable orthorhombic phase to the high temperature stable tetragonal phase. This phase change results from a change in tilt angle of the PbI_6^{4-} octahedra relative to the pseudocubic structure of the MA^+ cation[82,105,106]. An emission maximum of 1.67 eV at 0 K is received when extrapolating the values at a lower temperature.

3.5.5. Summary

A summary of the results for the exciton binding energy of PNPs with different compositions can be found in **Table 7**.

Table 7: Results for fitting the normalised integrated intensity as a function of temperature.

Composition	A / a.u.	E_B / meV	R^2
$MAPbBr_3$	142.4	43.6	0.9353
$MAPbBr_2I$	84.7	72.8	0.9906
$MAPbBrI_2$	25.3	73.1	0.9759
$MAPbBr_{0.5}I_{2.5}$	78.8	92.3	0.9846
$MAPbI_3$	87.2	104.0	0.9892

As can be seen from **Table 7**, the exciton binding energy increases with rising iodide content. This is contradictory to reports in literature, where the exciton binding energy decreases with increasing iodide content of the particles[92,102,103]. However, the opposite trend has been reported before[96] and it is well known that synthesis methods and conditions strongly influence the properties of PNPs. Therefore, further investigation of this phenomenon would be needed. However, all measured samples display exciton binding energies larger than that of bulk material, confirming quantum confinement of the synthesised material[93].

A comparison of the fitting parameters for FWHM as a function of temperature can be found in **Table 8**.

Table 8: Fitting parameters for FWHM in dependence on the temperature of different compositions of PNPs.

Composition	σ / eV K^{-1}	Γ_0 / meV	Γ_{op} / meV	E / meV	R^2
$MAPbBr_3$	$-5.04 \cdot 10^{-4}$	120.8	48.0	6.5	0.9700
$MAPbBr_2I$	$-2.60 \cdot 10^{-5}$	118.1	160.3	33.8	0.9875
$MAPbBrI_2$	$-3.51 \cdot 10^{-5}$	53.8	130.6	22.9	0.9882
$MAPbI_3$	$-1.55 \cdot 10^{-4}$	118.6	96.6	18.1	0.9554

As shown in **Table 8**, values for Γ_0 are similar in magnitude for all samples, except for $MAPbBrI_2$. This term measures the inhomogeneous, temperature-independent line broadening or the FWHM at 0 K. It is caused by fluctuations in the particles' size, shape and composition. Hence, it seems as though $MAPbBrI_2$ is the most uniform sample of the ones investigated, featuring the least size distribution and the smallest line width[99,107,108].

The homogeneous contribution to FWHM rises with increasing iodine content, as does the phonon energy participating in the quenching process. This is not surprising, as the PLQY value for fully bromide particles was substantially higher than that of iodide containing particles.

A summary of the shift in emission maxima at low temperatures can be found in **Table 9**.

Table 9: Energy of emission maximum at 0 K and rate of energy increase in dependence on the temperature at low temperatures.

Composition	E_0 / eV	$\delta E\, \delta T^{-1}$ / eV K^{-1}	R^2
$MAPbBr_3$	2.35	0.41	0.9883
$MAPbBr_2I$	2.28	0.32	0.9885
$MAPbBrI_2$	1.81	0.33	0.9988
$MAPbI_3$	1.67	0.35	0.9923

When looking at **Table 9**, the emission maximum decreases with increasing iodine content, as is expected. The rate of this decrease varies slightly, being somewhat smaller for mixed halide PNPs compared to the pure composition. However, this variance is neglectable and within the variation of the measurement.

3.6. Time-Resolved Spectroscopy

To gain further insight into the characteristics of the nanoparticles, time-resolved temperature dependent spectroscopy has been performed. The mixed halide PNPs with an iodide content of 33 % were omitted from this method, due to their low PLQY. The fluorescence lifetime curve may be fitted with either a mono- or bi-exponential decay process, displayed in **Equations 6** and **7**[80].

$$I(t) = I_0 + A_1 e^{-t/t_1} \quad \text{(Eq. 6)}$$

$$I(t) = I_0 + A_1 e^{-t/t_1} + A_2 e^{-t/t_2} \quad \text{(Eq. 7)}$$

with: I_0 = offset of the normalised intensity

A_1, A_2 = relative weight

t_1, t_2 = lifetime

All curves were fit with mono- and bi-exponential decays, with the appropriated decay identified using the coefficient of determination. While the mono-exponential decay yields only a single lifetime, the bi-exponential decay yields two individual lifetimes, a short and a long one, often attributed to two different processes[91].

3.6.1. $MAPbBr_3$

A fully bromide thin film sample was measured using time-resolved spectroscopy, with the results depicted in **Figure 27**.

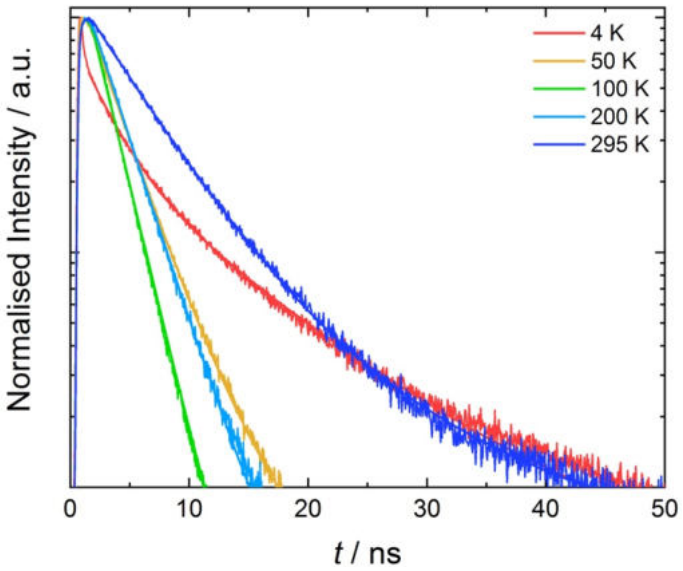

Figure 27: Time-resolved spectroscopy of a $MAPbBr_3$ thin film sample and exponential decay fit. The intensity was detected at 529 (4 K), 525 (50 K), 520 (100 K), 513 (200 K) and 510 nm (295 K).

When looking at **Figure 27**, interestingly long lifetimes can be found both at room temperature and 4 K, with the lifetime decreasing between these two temperatures. The shortest fluorescence lifetime was found at 100 K, with 2.05 ns. This point coincides with the phase transition temperature between the tetragonal and the orthorhombic phase.

Initially a rapid, mono-exponential decay is found at 4 K, which later on transitions into a bi-exponential decay with very high lifetimes, comparable to lifetimes at room temperature. The exact values received from fitting the spectra are listed in **Table 10**.

Table 10: Decay parameters of the $MAPbBr_3$ nanoparticles.

T / K	I_0 / a.u.	A_1 / a.u.	t_1 / ns	A_2 / a.u.	t_2 / ns
4	0.48	60.37	2.77	26.86	11.13
50	0.23	158.63	3.02	-	-
100	0.11	221.44	2.05	-	-
200	0.19	182.29	2.79	-	-
295	0.37	127.20	5.22	8.62	16.38

As can be seen, the rapid processes between 50 and 200 K follow a mono-exponential curve, while the fluorescence at room temperature and 4 K follows a bi-exponential decay. The slow component contributes more strongly to the overall lifetime at low temperatures, contributing 31 % compared to only 6 % at room temperature.

3.6.2. $MAPbBrI_2$

Using time-resolved spectroscopy, a mixed halide thin film sample with 66 % iodide content has been measured. The results are depicted in **Figure 28**.

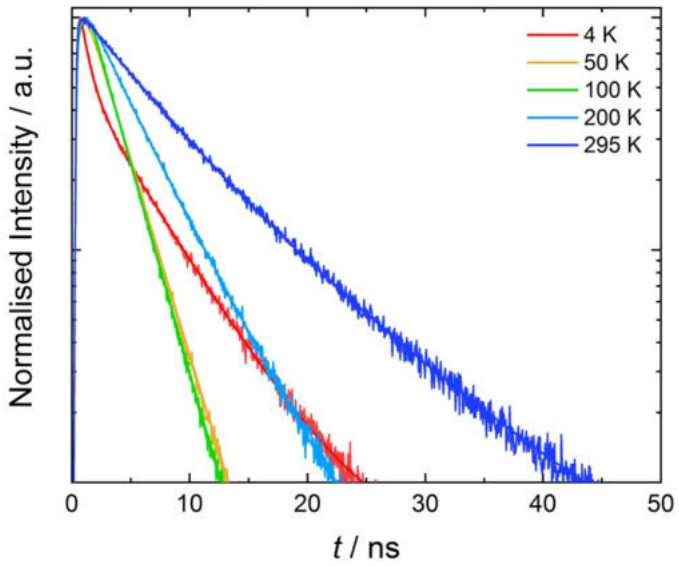

Figure 28: Time-resolved spectra of a $MAPbBrI_2$ thin film sample and fitting using a mono- or bi-exponential decay. The detected wavelength was set to 676 (4 K), 673 (50 K), 668 (100 K), 664 (200 K) and 659 nm (295 K).

As can be seen, this sample follows a different trend than the fully bromide particles. While the decay is still fastest at room temperature, it declines linearly with the temperature. At 4 K, a rapid, mono-exponential decline is initially present, which later turns into a bi-exponential decay. The exact parameters extracted from fitting the spectra are listed in **Table 11**.

Table 11: Parameters characterising the fluorescence decay of a $MAPbBrI_2$ thin film sample.

T / K	I_0 / a.u.	A_1 / a.u.	t_1 / ns	A_2 / a.u.	t_2 / ns
4	0.48	125.97	0.82	58.23	5.25
50	0.04	168.97	2.58	-	-
100	0.04	189.59	2.40	-	-
200	0.14	140.89	4.22	-	-
295	0.02	84.92	6.04	30.39	12.18

When observing **Table 11**, similar to $MAPbBr_3$ a bi-exponential decay process is found for room temperature and 4 K, while between 50 and 200 K, a mono-exponential decay prevails. Furthermore, the fastest fluorescence is found at 100 K, correlating with the phase transition observed through low-temperature, steady-state spectroscopy.

3.6.3. $MAPbI_3$

To fully determine the impact of iodide on the fluorescence lifetime, a purely iodide $MAPbI_3$ has been studied using time-resolved temperature-dependent spectroscopy. The results are depicted in **Figure 29**.

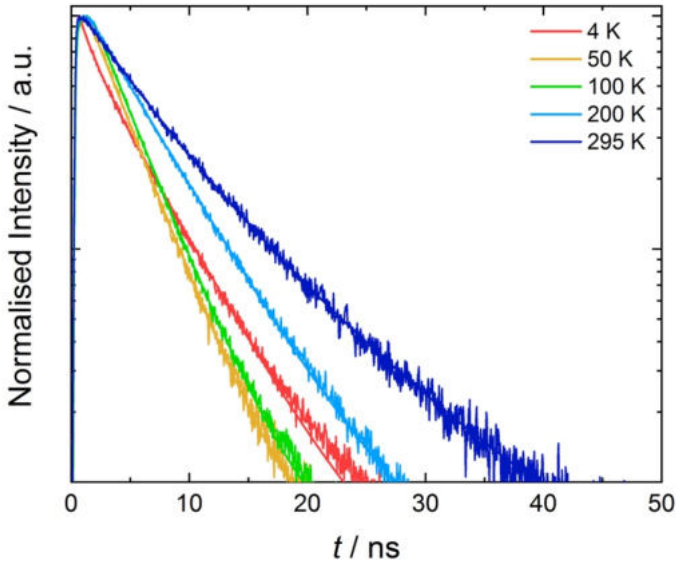

Figure 29: Time-resolved temperature-dependent spectroscopy of a fully iodide $MAPbI_3$ thin film sample. The fluorescence was detected at 723 (4 K), 721 (50 and 100 K), 735 (200 K) and 719 nm (295 K).

As shown in **Figure 29**, the decay process follows the temperature linearly at low lifetimes, decreasing step by step. However, a slow decay process is visible at 4 K, resulting in a longer fluorescence lifetime compared to 50 or 100 K. As has been found previously, the shortest fluorescence lifetime can be seen around the transition temperature between the room temperature stable tetragonal configuration and the low temperature stable orthorhombic phase. The decay parameters resulting from fitting the spectra are depicted in **Table 12**.

Table 12: Decay parameters of a fully iodide $MAPbI_3$ thin film sample.

T / K	I_0 / a.u.	A_1 / a.u.	t_1 / ns
4	0.44	108.16	4.09
50	0.23	151.45	3.34
100	0.20	156.90	3.55
200	0.21	132.42	5.11
295	0.57	112.28	6.68

As can be seen, $MAPbI_3$ proved to be the only sample that could be fitted with a mono-exponential decay over the whole temperature range. Thus, lifetimes can be easily compared, as they only feature a single decay process. It is found that the lifetime minimises between 50 and 100 K as the phase transition occurs and increases again at room temperature. As was already suspected through low-temperature spectroscopical studies depicted in **Figure 26**, the

probability of carriers being caught in trap-states and thus depleting the emission intensity and increasing the lifetime is considerably less around the phase transition as compared to other temperatures. Furthermore, no clear trend can be found when looking at fluorescence lifetime dependence on iodide content.

4. Conclusion

This thesis successfully uses the LARP method to prepare red emissive MA-based perovskite nanoparticles. Using the starting materials MABr and PbI_2, the synthesis method was fine-tuned to produce mixed halide PNPs with 66 % iodide, depicting a mean emission of 672 nm and a mean PLQY of 45 % in thin film samples. Interestingly, when precipitating the particles from toluene, no perovskite structure and thus no emission is formed, as only white particles are received. After annealing the samples at 120 °C, a colour change is induced as the perovskite structure is formed and an emission is received. Surprisingly, the exact temperature did not show a noticeable effect, however, all compositions benefit from prolonged exposure to heat, with all samples increasing in PLQY and displaying a bathochromic shift.

Furthermore, it was found that the PNPs display an extraordinary tolerance towards water. Even when water contamination is present within the precursor solution or during the precipitation, no change in properties can be found. Thus, neither anhydrous solvents nor an inert atmosphere is needed when producing these nanoparticles. Moreover, the nanoparticles proved to be highly stable as thin film samples, only losing 5 % of the initial PLQY value over 30 days. This outstanding stability is achieved without encapsulation of the particles while stored under ambient conditions at room temperature.

Successively increasing the iodide content in the various PNP samples yielded the desired band gap shift to lower energies by a value of 0.58 eV from fully bromide to fully iodide particles. The excitonic behaviour was studied using low-temperature spectroscopy, with an increase in exciton binding energy found upon raising the iodide content. All samples studied yielded the perovskite typical hypsochromic shift with increasing temperature. Furthermore, the mixed halide sample with 66 % iodide content displayed an exceptionally small inhomogeneous line broadening, indicative of a uniquely homogeneous sample in composition, size and shape.

Stable PNPs can be produced using this synthesis approach, displaying high fluorescence emission over the whole visible spectrum. These properties make the nanoparticles ideal candidates for use in optoelectronic devices, such as highly-efficient quantum-dot-based LEDs.

5. Appendix

Table 13: List of chemicals used in this work.

Chemical	Abbreviation	*M* / g mol^{-1}	*Purity* / %	Manufacturer
Dimethylformamide	DMF	73.09	99.8	Sigma-Aldrich
Formamidinium bromide	FABr	124.97		
Formamidinium iodide	FAI	171.97		
Hexanoic acid	HeA	116.16	≥ 99	Sigma-Aldrich
Lead bromide	$PbBr_2$	367.01	99.99	Sigma-Aldrich
Lead iodide	PbI_2	461.00	99.99	Alfa Aesar
Methylammonium bromide	MABr	111.97		Greatcell Solar Materials
Methylammonium iodide	MAI	158.97		
*t*boc-Lysine		246.30	97	Roth
Toluene		92.14		VWR

6. List of Figures

7. List of Tables

8. Literature

1. Taylor, A. D. *et al.* A general approach to high-efficiency perovskite solar cells by any antisolvent. *Nature Communications* **12**, 1–11 (2021).
2. Pan, H., Shao, H., Zhang, X. L., Shen, Y. & Wang, M. Interface engineering for high-efficiency perovskite solar cells. *Journal of Applied Physics* **129**, 1–9 (2021).
3. Xiong, S. *et al.* Defect passivation by nontoxic biomaterial yields 21% efficiency perovskite solar cells. *Journal of Energy Chemistry* **55**, 265–271 (2021).
4. Cheng, M. *et al.* Full visible waveband tunable formamidinium halides hybrid perovskite QDs via anion-exchange route and their high luminous efficiency LEDs. *Journal of Alloys and Compounds* **791**, 814–821 (2019).
5. Zhang, T. *et al.* Room-temperature synthesized formamidinium lead halide perovskite quantum dots with bright luminescence and color-tunability for efficient light emitting. *Organic Electronics* **68**, 76–84 (2019).
6. Hassan, Y. *et al.* Ligand-engineered bandgap stability in mixed-halide perovskite LEDs. *Nature* **591**, 72–77 (2021).
7. Chiba, T. *et al.* Anion-exchange red perovskite quantum dots with ammonium iodine salts for highly efficient light-emitting devices. *Nature Photonics* **12**, 681–687 (2018).
8. Guhrenz, C. *et al.* Solid-State Anion Exchange Reactions for Color Tuning of $CsPbX_3$ Perovskite Nanocrystals. *Chemistry of Materials* **28**, 9033–9040 (2016).
9. Akkerman, Q. A., Rainò, G., Kovalenko, M. v. & Manna, L. Genesis, challenges and opportunities for colloidal lead halide perovskite nanocrystals. *Nature Materials* **17**, 394–405 (2018).

10. Bi, C. *et al.* Room-Temperature Construction of Mixed-Halide Perovskite Quantum Dots with High Photoluminescence Quantum Yield. *Journal of Physical Chemistry C* **122**, 5151–5160 (2018).
11. Chen, D., Li, J., Chen, X., Chen, J. & Zhong, J. Grinding Synthesis of $APbX_3$ (A = MA, FA, Cs; X = Cl, Br, I) Perovskite Nanocrystals. *ACS Applied Materials and Interfaces* **11**, 10059–10067 (2019).
12. Hassan, Y. *et al.* Facile Synthesis of Stable and Highly Luminescent Methylammonium Lead Halide Nanocrystals for Efficient Light Emitting Devices. *J Am Chem Soc* **141**, 1269–1279 (2019).
13. Huang, H., Bodnarchuk, M. I., Kershaw, S. v., Kovalenko, M. v. & Rogach, A. L. Lead Halide Perovskite Nanocrystals in the Research Spotlight: Stability and Defect Tolerance. *ACS Energy Letters* **2**, 2071–2083 (2017).
14. Das, S. & Samanta, A. Highly Luminescent and Phase-Stable Red/NIR-Emitting All-Inorganic and Hybrid Perovskite Nanocrystals. *ACS Energy Letters* **6**, 3780–3787 (2021).
15. Wu, X. G. *et al.* Highly luminescent red emissive perovskite quantum dots-embedded composite films: Ligands capping and caesium doping-controlled crystallization process. *Nanoscale* **11**, 4942–4947 (2019).
16. Zhang, C. *et al.* A deep-dyeing strategy for ultra-stable, brightly luminescent perovskite-polymer composites. *Journal of Materials Chemistry C* **9**, 3396–3402 (2021).
17. Kovalenko, M. v., Protesescu, L. & Bodnarchuk, M. I. Properties and potential optoelectronic applications of lead halide perovskite nanocrystals. *Science (1979)* **358**, 745–750 (2017).
18. Protesescu, L. *et al.* Dismantling the “red Wall” of Colloidal Perovskites: Highly Luminescent Formamidinium and Formamidinium-Cesium Lead Iodide Nanocrystals. *ACS Nano* **11**, 3119–3134 (2017).
19. Zhenfu, Z., Zhihai, W., Jiong, C., Liang, J. & Yafei, H. Nanocomposites of Perovskite Quantum Dots Embedded in Magnesium Silicate Hollow Spheres for Multicolor Display. *Journal of Physical Chemistry C* **122**, 16887–16893 (2018).
20. Levchuk, I. *et al.* Brightly Luminescent and Color-Tunable Formamidinium Lead Halide Perovskite $FAPbX_3$ (X = Cl, Br, I) Colloidal Nanocrystals. *Nano Letters* **17**, 2765–2770 (2017).
21. Veldhuis, S. A. *et al.* Perovskite Materials for Light-Emitting Diodes and Lasers. *Advanced Materials* **28**, 6804–6834 (2016).
22. Jancik Prochazkova, A. *et al.* Controlling Quantum Confinement in Luminescent Perovskite Nanoparticles for Optoelectronic Devices by the Addition of Water. *ACS Applied Nano Materials* **3**, 1242–1249 (2020).
23. Jancik Prochazkova, A. *et al.* Synthesis conditions influencing formation of $MAPbBr_3$ perovskite nanoparticles prepared by the ligand-assisted precipitation method. *Scientific Reports* **10**, 15720 (2020).
24. Chakhmouradian, A. R. & Woodward, P. M. Celebrating 175 years of perovskite research: A tribute to Roger H. Mitchell. *Physics and Chemistry of Minerals* **41**, 387–391 (2014).

25. Jena, A. K., Kulkarni, A. & Miyasaka, T. Halide Perovskite Photovoltaics: Background, Status, and Future Prospects. *Chemical Reviews* **119**, 3036–3103 (2019).
26. Bhalla, A. S., Guo, R. & Roy, R. The perovskite structure - A review of its role in ceramic science and technology. *Materials Research Innovations* **4**, 3–26 (2000).
27. R. E. Cohen. Origin of ferroelectricity in perovskite oxides. *Nature* **359**, 136–138 (1992).
28. Peña, M. A. & Fierro, J. L. G. Chemical structures and performance of perovskite oxides. *Chemical Reviews* **101**, 1981–2017 (2001).
29. Akkerman, Q. A. & Manna, L. What Defines a Halide Perovskite? *ACS Energy Letters* **5**, 604–610 (2020).
30. Saparov, B. & Mitzi, D. B. Organic-Inorganic Perovskites: Structural Versatility for Functional Materials Design. *Chemical Reviews* **116**, 4558–4596 (2016).
31. Matsushita, N., Kitagawa, H. & Kojima, N. A three-dimensional iodo-bridged mixed-valence gold(I,III) compound, $Cs_2Au^{I}Au^{III}I_6$. *Acta Crystallographica Section C: Crystal Structure Communications* **53**, 663–666 (1997).
32. Mitzi, D. B. Templating and structural engineering in organic-inorganic perovskites. *Journal of the Chemical Society, Dalton Transactions* **1**, 1–12 (2001).
33. Kang, J. & Wang, L. W. High Defect Tolerance in Lead Halide Perovskite $CsPbBr_3$. *Journal of Physical Chemistry Letters* **8**, 489–493 (2017).
34. Hu, Y. L. *et al.* Rapid synthesis of cesium lead halide perovskite nanocrystals by L-lysine assisted solid-phase reaction at room temperature. *RSC Advances* **10**, 34215–34224 (2020).
35. Kulkarni, S. A., Mhaisalkar, S. G., Mathews, N. & Boix, P. P. Perovskite Nanoparticles: Synthesis, Properties, and Novel Applications in Photovoltaics and LEDs. *Small Methods* **3**, 1–16 (2019).
36. Huang, J., Tan, S., Lund, P. D. & Zhou, H. Impact of H_2O on organic-inorganic hybrid perovskite solar cells. *Energy and Environmental Science* **10**, 2284–2311 (2017).
37. Wei, Y., Cheng, Z. & Lin, J. An overview on enhancing the stability of lead halide perovskite quantum dots and their applications in phosphor-converted LEDs. *Chemical Society Reviews* **48**, 310–350 (2019).
38. Xi, L. *et al.* Facile in situ synthesis of stable luminescent organic-inorganic lead halide perovskite nanoparticles in a polymer matrix. *Journal of Materials Chemistry C* **5**, 7207–7214 (2017).
39. Huang, S. *et al.* Enhancing the Stability of $CH_3NH_3PbBr_3$ Quantum Dots by Embedding in Silica Spheres Derived from Tetramethyl Orthosilicate in “waterless” Toluene. *J Am Chem Soc* **138**, 5749–5752 (2016).
40. Wu, H., Lin, S., Wang, R., You, X. & Chi, Y. Water-stable and ion exchange-free inorganic perovskite quantum dots encapsulated in solid paraffin and their application in light emitting diodes. *Nanoscale* **11**, 5557–5563 (2019).
41. Sun, C. *et al.* Efficient and Stable White LEDs with Silica-Coated Inorganic Perovskite Quantum Dots. *Advanced Materials* **28**, 10088–10094 (2016).
42. Wei, Y. *et al.* Enhancing the Stability of Perovskite Quantum Dots by Encapsulation in Crosslinked Polystyrene Beads via a Swelling–Shrinking Strategy toward Superior Water Resistance. *Advanced Functional Materials* **27**, 1–8 (2017).

43. Matura, K. Embedding of highly-fluorescent perovskite nanoparticles into transparent polymeric matrices. (2021).
44. Kamat, P. v. & Kuno, M. Halide Ion Migration in Perovskite Nanocrystals and Nanostructures. *Accounts of Chemical Research* **54**, 520–531 (2021).
45. Yuan, Y. & Huang, J. Ion Migration in Organometal Trihalide Perovskite and Its Impact on Photovoltaic Efficiency and Stability. *Accounts of Chemical Research* **49**, 286–293 (2016).
46. Zhang, H. *et al.* Phase segregation due to ion migration in all-inorganic mixed-halide perovskite nanocrystals. *Nature Communications* **10**, 1–8 (2019).
47. Zhang, T., Hu, C. & Yang, S. Ion Migration: A “Double-Edged Sword” for Halide-Perovskite-Based Electronic Devices. *Small Methods* **4**, 1–20 (2020).
48. Akkerman, Q. A. *et al.* Tuning the optical properties of cesium lead halide perovskite nanocrystals by anion exchange reactions. *J Am Chem Soc* **137**, 10276–10281 (2015).
49. Jiang, M., Hu, Z., Ono, L. K. & Qi, Y. $CsPbBr_xI_{3-x}$ thin films with multiple ammonium ligands for low turn-on pure-red perovskite light-emitting diodes. *Nano Research* **14**, 191–197 (2021).
50. Huang, H. *et al.* Top-Down Fabrication of Stable Methylammonium Lead Halide Perovskite Nanocrystals by Employing a Mixture of Ligands as Coordinating Solvents. *Angewandte Chemie* **129**, 9699–9704 (2017).
51. Martínez-Sarti, L. *et al.* Low-dimensional iodide perovskite nanocrystals enable efficient red emission. *Nanoscale* **11**, 12793–12797 (2019).
52. Minh, D. N. *et al.* Room-Temperature Synthesis of Widely Tunable Formamidinium Lead Halide Perovskite Nanocrystals. *Chemistry of Materials* **29**, 5713–5719 (2017).
53. Hills-Kimball, K., Yang, H., Cai, T., Wang, J. & Chen, O. Recent Advances in Ligand Design and Engineering in Lead Halide Perovskite Nanocrystals. *Advanced Science* **8**, 1–43 (2021).
54. Yoon, S. J., Stamplecoskie, K. G. & Kamat, P. v. How Lead Halide Complex Chemistry Dictates the Composition of Mixed Halide Perovskites. *Journal of Physical Chemistry Letters* **7**, 1368–1373 (2016).
55. Marongiu, D. *et al.* Self-Assembled Lead Halide Perovskite Nanocrystals in a Perovskite Matrix. *ACS Energy Letters* **2**, 769–775 (2017).
56. Leeb, E. Synthesis Optimization of Lead Bromide Perovskite Nanoparticles. (2020).
57. Jancik Prochazkova, A. *et al.* Cyclic Peptide Stabilized Lead Halide Perovskite Nanoparticles. *Scientific Reports* **9**, 3–8 (2019).
58. Jancik Prochazkova, A. *et al.* Proteinogenic Amino Acid Assisted Preparation of Highly Luminescent Hybrid Perovskite Nanoparticles. *ACS Applied Nano Materials* **2**, 4267–4274 (2019).
59. Huang, H., Susha, A. S., Kershaw, S. v., Hung, T. F. & Rogach, A. L. Control of Emission Color of High Quantum Yield $CH_3NH_3PbBr_3$ Perovskite Quantum Dots by Precipitation Temperature. *Advanced Science* **2**, 1–5 (2015).
60. Zhang, Z. Y. *et al.* The role of trap-assisted recombination in luminescent properties of organometal halide $CH_3NH_3PbBr_3$ perovskite films and quantum dots. *Scientific Reports* **6**, 1–7 (2016).

61. Scheidt, R. A., Atwell, C. & Kamat, P. v. Tracking Transformative Transitions: From $CsPbBr_3$ Nanocrystals to Bulk Perovskite Films. *ACS Materials Letters* **1**, 8–13 (2019).
62. Juarez-Perez, E. J., Hawash, Z., Raga, S. R., Ono, L. K. & Qi, Y. Thermal degradation of $CH_3NH_3PbI_3$ perovskite into NH_3 and CH_3I gases observed by coupled thermogravimetry-mass spectrometry analysis. *Energy and Environmental Science* **9**, 3406–3410 (2016).
63. Mayr, F. Optical Characterization of Organic and Perovskite Semiconductors by Photothermal Deflection Spectroscopy. (2020).
64. Tolouei nia, P. *et al.* Moisture-Induced Structural Degradation in Methylammonium Lead Iodide Perovskite Thin Films. *ACS Applied Energy Materials* **3**, 8240–8248 (2020).
65. Huang, J., Tan, S., Lund, P. D. & Zhou, H. Impact of H2O on organic-inorganic hybrid perovskite solar cells. *Energy and Environmental Science* **10**, 2284–2311 (2017).
66. Ge, Q. Q. *et al.* Promoting crystalline grain growth and healing pinholes by water vapor modulated post-annealing for enhancing the efficiency of planar perovskite solar cells. *Journal of Materials Chemistry A* **4**, 13458–13467 (2016).
67. Wang, M., Sun, H., Cao, F., Tian, W. & Li, L. Moisture-Triggered Self-Healing Flexible Perovskite Photodetectors with Excellent Mechanical Stability. *Advanced Materials* **33**, 1–8 (2021).
68. Zhou, W. *et al.* Reversible Healing Effect of Water Molecules on Fully Crystallized Metal-Halide Perovskite Film. *Journal of Physical Chemistry C* **120**, 4759–4765 (2016).
69. Müller, C. *et al.* Water Infiltration in Methylammonium Lead Iodide Perovskite: Fast and Inconspicuous. *Chemistry of Materials* **27**, 7835–7841 (2015).
70. Aamir, M., Sher, M., Malik, M. A., Revaprasadu, N. & Akhtar, J. A facile approach for selective and sensitive detection of aqueous contamination in DMF by using perovskite material. *Materials Letters* **183**, 135–138 (2016).
71. Makuła, P., Pacia, M. & Macyk, W. How To Correctly Determine the Band Gap Energy of Modified Semiconductor Photocatalysts Based on UV-Vis Spectra. *Journal of Physical Chemistry Letters* **9**, 6814–6817 (2018).
72. Sarritzu, V. *et al.* Direct or Indirect Bandgap in Hybrid Lead Halide Perovskites? *Advanced Optical Materials* **6**, 1–8 (2018).
73. Castelli, I. E., García-Lastra, J. M., Thygesen, K. S. & Jacobsen, K. W. Bandgap calculations and trends of organometal halide perovskites. *APL Materials* **2**, 1–7 (2014).
74. Roy, M. *et al.* Composition-Controlled Synthesis of Hybrid Perovskite Nanoparticles by Ionic Metathesis: Bandgap Engineering Studies from Experiments and Theoretical Calculations. *Chemistry - A European Journal* **25**, 9892–9901 (2019).
75. Sadhukhan, P. *et al.* Solvent-Free Solid-State Synthesis of High Yield Mixed Halide Perovskites for Easily Tunable Composition and Band Gap. *Crystal Growth and Design* **18**, 3428–3432 (2018).
76. Ou, Q. *et al.* Band structure engineering in metal halide perovskite nanostructures for optoelectronic applications. *Nano Materials Science* **1**, 268–287 (2019).

77. Longo, G. *et al.* Fully Vacuum-Processed Wide Band Gap Mixed-Halide Perovskite Solar Cells. *ACS Energy Letters* **3**, 214–219 (2018).
78. Schuster, O. *et al.* Looking beyond the Surface: The Band Gap of Bulk Methylammonium Lead Iodide. *Nano Letters* **20**, 3090–3097 (2020).
79. Naghadeh, S. B. *et al.* Size and temperature dependence of photoluminescence of hybrid perovskite nanocrystals. *Journal of Chemical Physics* **151**, 1–9 (2019).
80. Yi, J. *et al.* The correlation between phase transition and photoluminescence properties of $CsPbX_3$ (X = Cl, Br, I) perovskite nanocrystals. *Nanoscale Advances* **2**, 4390–4394 (2020).
81. Varshni, Y. P. Temperature dependence of the energy gap in semiconductors. *Physica* **34**, 149–154 (1967).
82. Dar, M. I. *et al.* Origin of unusual bandgap shift and dual emission in organic-inorganic lead halide perovskites. *Science Advances* **2**, 1–9 (2016).
83. Hou, L., Tamarat, P. & Lounis, B. Revealing the exciton fine structure in lead halide perovskite nanocrystals. *Nanomaterials* **11**, (2021).
84. Wu, K. *et al.* Temperature-dependent excitonic photoluminescence of hybrid organometal halide perovskite films. *Physical Chemistry Chemical Physics* **16**, 22476–22481 (2014).
85. Lee, S. M. *et al.* Temperature-Dependent Photoluminescence of Cesium Lead Halide Perovskite Quantum Dots: Splitting of the Photoluminescence Peaks of $CsPbBr_3$ and $CsPb(Br/I)_3$ Quantum Dots at Low Temperature. *Journal of Physical Chemistry C* **121**, 26054–26062 (2017).
86. Youn, C. J., Jeong, T. S., Han, M. S. & Kim, J. H. Optical properties of Zn-terminated ZnO bulk. *Journal of Crystal Growth* **261**, 526–532 (2004).
87. Ahumada-Lazo, R. *et al.* Exciton effects in perovskite nanocrystals. *Journal of Physics: Photonics* **3**, 1–11 (2021).
88. Zheng, K. *et al.* Exciton Binding Energy and the Nature of Emissive States in Organometal Halide Perovskites. *Journal of Physical Chemistry Letters* **6**, 2969–2975 (2015).
89. Strzałkowski, K., Zakrzewski, J. & Maliński, M. Determination of the exciton binding energy using photothermal and photoluminescence spectroscopy. *International Journal of Thermophysics* **34**, 691–700 (2013).
90. Li, F. *et al.* Enhancing exciton binding energy and photoluminescence of formamidinium lead bromide by reducing its dimensions to 2D nanoplates for producing efficient light emitting diodes. *Nanoscale* **10**, 20611–20617 (2018).
91. Shinde, A., Gahlaut, R. & Mahamuni, S. Low-Temperature Photoluminescence Studies of $CsPbBr_3$ Quantum Dots. *Journal of Physical Chemistry C* **121**, 14872–14878 (2017).
92. Yang, Y. *et al.* Comparison of Recombination Dynamics in $CH_3NH_3PbBr_3$ and $CH_3NH_3PbI_3$ Perovskite Films: Influence of Exciton Binding Energy. *Journal of Physical Chemistry Letters* **6**, 4688–4692 (2015).
93. Galkowski, K. *et al.* Determination of the exciton binding energy and effective masses for methylammonium and formamidinium lead tri-halide perovskite semiconductors. *Energy and Environmental Science* **9**, 962–970 (2016).

94. Turyanska, L., Patanè, A., Henini, M., Hennequin, B. & Thomas, N. R. Temperature dependence of the photoluminescence emission from thiol-capped PbS quantum dots. *Applied Physics Letters* **90**, 2–4 (2007).
95. Wen, X., van Dao, L. & Hannaford, P. Temperature dependence of photoluminescence in silicon quantum dots. *Journal of Physics D: Applied Physics* **40**, 3573–3578 (2007).
96. Demchyshyn, S. Quantum confinement effects for light emission in perovskites. (2018).
97. D'Innocenzo, V. *et al.* Excitons versus free charges in organo-lead tri-halide perovskites. *Nature Communications* **5**, 1–6 (2014).
98. Xing, G. *et al.* Low-temperature solution-processed wavelength-tunable perovskites for lasing. *Nature Materials* **13**, 476–480 (2014).
99. Woo, H. C. *et al.* Temperature-Dependent Photoluminescence of $CH_3NH_3PbBr_3$ Perovskite Quantum Dots and Bulk Counterparts. *Journal of Physical Chemistry Letters* **9**, 4066–4074 (2018).
100. Xu, Q. *et al.* Low-temperature photoluminescence spectroscopy of $CH_3NH_3PbBr_xCl_{3-x}$ perovskite single crystals. *Journal of Alloys and Compounds* **792**, 185–190 (2019).
101. Phuong, L. Q. *et al.* Free Carriers versus Excitons in $CH_3NH_3PbI_3$ Perovskite Thin Films at Low Temperatures: Charge Transfer from the Orthorhombic Phase to the Tetragonal Phase. *Journal of Physical Chemistry Letters* **7**, 2316–2321 (2016).
102. Makarov, S. *et al.* Halide-Perovskite Resonant Nanophotonics. *Advanced Optical Materials* **7**, 1–19 (2019).
103. Kitazawa, N., Watanabe, Y. & Nakamura, Y. Optical properties of $CH_3NH_3PbX_3$ (X = halogen) and their mixed-halide crystals. **7**, 3585–3587 (2002).
104. Parveen, S., Paul, K. K., Das, R. & Giri, P. K. Large exciton binding energy, high photoluminescence quantum yield and improved photostability of organo-metal halide hybrid perovskite quantum dots grown on a mesoporous titanium dioxide template. *Journal of Colloid and Interface Science* **539**, 619–633 (2019).
105. Kong, W. *et al.* Characterization of an abnormal photoluminescence behavior upon crystal-phase transition of perovskite $CH_3NH_3PbI_3$. *Physical Chemistry Chemical Physics* **17**, 16405–16411 (2015).
106. Milot, R. L., Eperon, G. E., Snaith, H. J., Johnston, M. B. & Herz, L. M. Temperature-Dependent Charge-Carrier Dynamics in $CH_3NH_3PbI_3$ Perovskite Thin Films. *Advanced Functional Materials* **25**, 6218–6227 (2015).
107. Morello, G. *et al.* Temperature and size dependence of nonradiative relaxation and exciton-phonon coupling in colloidal CdTe quantum dots. *Journal of Physical Chemistry C* **111**, 5846–5849 (2007).
108. Shamsi, J., Urban, A. S., Imran, M., de Trizio, L. & Manna, L. Metal Halide Perovskite Nanocrystals: Synthesis, Post-Synthesis Modifications, and Their Optical Properties. *Chemical Reviews* **119**, 3296–3348 (2019).